JOÃO SOUSA LUIS

Licenciado em Ciências de Engenharia de Micro e Nanotecnologia

MICROSTRUCTURED TRANSPARENT CONDUCTIVE METALLIC ELECTRODES FABRICATED BY COLLOIDAL LITHOGRAPHY

Dissertação para obtenção do Grau de Mestre em Engenharia de Micro e Nanotecnologias

Orientador: Manuel João de Moura Dias Mendes, Senior Researcher, Departamento de Ciências dos Materiais, Faculdade de Ciências e Tecnologias da Universidade Nova de Lisboa

Co-orientador: Olalla Sanchez-Sobrado,Post-doctoral Researcher, Departamento de Ciências dos Materiais, Faculdade de Ciências e Tecnologias da Universidade Nova de Lisboa

Júri: *(Font: Arial, 10 pt normal)*

Presidente: Prof. Doutor(a) [Nome Completo]
Arguente(s): Prof. Doutor(a) [Nome Completo]
Vogal(ais): Prof. Doutor(a) [Nome Completo]

FACULDADE DE CIÊNCIAS E TECNOLOGIA
UNIVERSIDADE NOVA DE LISBOA

Abril 2018

Microstructured transparent conductive metallic electrodes fabricated by colloidal lithography

“Whether you think you can or you can’t – you’re right.”

– Henry Ford

Acknowledgements

É com enorme satisfação que agradeço a todos os que me ofereceram apoio nos melhores e piores momentos da maior etapa da minha vida e contribuíram para o meu sucesso.

Em primeiro lugar gostaria ao Professor Dr. Rodrigo Martins e à Professora Dra. Elvira Fortunato pela criação e desenvolvimento do curso das Micro e Nanotecnologias e pelas condições oferecidas no CENIMAT|i3N e no CEMOP que proporcionam excelentes condições de trabalho.

Gostaria de deixar um grande agradecimento ao meu orientador, Professor Dr. Manuel João Mendes, por todo o apoio com literatura e pela ajuda a melhorar o meu trabalho e à minha co-orientadora, Dra. Olalla Sobral Sanchez, por todo o tempo que perdeu comigo a entrar e a sair da câmara limpa e pela formação em praticamente todos os equipamentos que usei durante a dissertação.

Ao Tiago Mateus e à Diana Gaspar que, sempre que necessitei, se mostraram disponíveis para perderem tempo comigo a quebrar vácuo e fazer vácuo e completar as deposições várias deposições.

À Alexandra Gonçalves e à Sónia pereira pela disponibilidade e por serem tão prestáveis a facultar material e ajudar nos laboratórios.

À Daniela Gomes por todas as sessões no SEM e ao Tomás Calmeiro pelas sessões no AFM.

A special thanks to Giacomo Torrissi for all the good times and help provided for the completion of this work.

Gostaria também de agradecer a todos os professores que proporcionaram as competências para encontrar e resolver problemas e sempre se mostraram disponíveis para ajudar no que fosse preciso.

Aos amigos de primeiro semestre, Daniela Magalhães e Sara Silvestre, que atravessaram esta última barreira comigo e a tornaram tão mais apreciável.

Queria aos companheiros de casa, João Crespo, David Esteves e Filipe Marque aka Caloiro Idiota, que proporcionaram os momentos mais aleatórios e divertidos dos últimos tempos. Desde o clássico agrupamento no hall de entrada à espera que o router funcionasse ao frango colado na parede.

À Inês Martins e ao Francisco Matos pelos momentos de procrastinação extrema no primeiro e segundo ano e aos bons momentos que passámos juntos ao longo dos anos.

Ao João Coroa, ao Tiago Gameiro e ao Shiv Bhudia pelos momentos de lazer, tanto as idas à Costa depois das aulas como os jogos à noite.

À Sissi, que me deu todo o apoio que alguma vez poderia pedir, mantendo-me no caminho para o sucesso especialmente nos momentos mais dificeis.

Aos meus irmãos e à minha por me terem acompanhado ao longo da vida e fazerem de mim a pessoa que sou hoje.

Muito obrigado a todos!

Abstract

This thesis focuses on the development and optimization of a technique known as self-assembly colloidal lithography (CL) to fabricate transparent conductive electrodes. These contacts are of utmost importance for high performance optoelectronic devices, such as thin film solar cells. As of this moment, indium tin oxide (ITO) is the preferred transparent conductive oxide (TCO), but to improve the cell efficiency new materials with lower sheet resistance and better optical properties should be used. Besides, ITO is relatively expensive, so alternative Earth-abundant materials are highly desired to improve the devices' cost-effectiveness. Conductive metallic micro-meshes within two thin TCO layers were investigated to improve the sheet resistance while maintaining an anti-reflection coating (ARC) type layer. The meshes were fabricated by CL after studying the influence of the main process parameters: polystyrene sphere sizes, etching times, aluminum and silver for the mesh and indium zinc oxide (IZO) and aluminum zinc oxide (AZO) for the TCO layer were studied. The resulting contacts were analyzed through UV-VIS-NIR spectrophotometry, hall-effect, scanning electron microscopy (SEM) equipped with energy dispersive spectroscopy (EDS) and atomic force microscopy (AFM). The results showed that 1.6 μm precursor spheres etched for 150s were the most reliable to produce closely-packed structures and to obtain low sheet resistance, while 5 μm spheres etched for 120s showed the best optical performance over the UV-VIS-NIR range. The contacts which showed the best optical and electrical results were produced with silver and IZO: when produced with 1.6 μm spheres the contacts presented sheet resistances as low as 10.6 Ω/sq and transmittances up to 75 %, and when produced with 5 μm spheres obtained transmittance up to 85 % with sheet resistance of 121 Ω/sq. The results reveal that our innovative large-area micro-meshed metallic electrodes fabricated by CL can attain performances close to those off state-of-art ITO (10 Ω/sq for 80 % transmittance and 100 Ω/sq for 90 % transmittance), but with superior transmittance mainly in the near-infrared range. This can be highly interesting, for instance, for the intermediate electrodes in multi-terminal multi-junction solar cell architectures.

Keywords: Transparent conductive electrode, Colloidal lithography, Langmuir-Blodgett, Self-Assembly, anti-reflection coating

Resumo

Esta tese foca-se no desenvolvimento e otimização de uma técnica conhecida como litografia coloidal de auto assemblagem para fabricação de elétrodos condutores transparentes. Estes contactos são importância extrema para dispositivos eletrónicos de alta performance, tais como células solares de filme fino. De momento, o óxido de índio dopado com estanho (ITO) é o óxido condutor transparente (TCO) preferido, mas de forma a melhorar a eficiência da célula novos materiais com menor resistência de folha e melhores propriedades óticas devem ser usados. Foi introduzida uma rede de metal entre duas camadas finas de TCO para melhorar a resistência de folha ao mesmo tempo que se mantêm a camada de anti reflexão (ARC). Tamanhos de esferas de polistireno, tempos de erosão, alumínio e prata para a rede e óxido de índio dopado com zinco (IZO) e óxido de alumínio dopado com zinco (AZO) para a camada de TCO foram estudados. Os contactos foram analisados através de espetrofotómetro de UV-VIS-NIR, efeito de Hall, microscópio eletrónico de varrimento (SEM) e microscópio de força atómica (AFM). Os resultados mostram que esferas de 1.6 μm erodidas durante 150 s foram as mais consistentes a produzir estruturas com maior empacotamento e menor resistência de folha, enquanto as esferas de 5 μm erodidas durante 120 s mostraram melhores capacidades óticas no espectro UV-VIS-NIR. Os contactos com melhores propriedades óticas e elétricas foram produzidos com prata e IZO: quando produzidos com esferas de 1.6 μm os contactos apresentaram resistências tão baixas quanto 10.6 Ω/quadrado e transmitâncias tão altas quanto 75 % e quando produzidos com esferas de 5 μm os contactos apresentaram transmitâncias tão altas quanto 85 % e resistência folha de 121 Ω/quadrado. Os resultados revelam que os nossos inovativos elétrodos *micromesh* metálicos de larga área fabricados por CL atingem performances próximas das do ITO estado da arte (10 Ω/sq a 80% transmitância e 100 Ω/sq a 90%), mas com muito melhor transmitância para comprimentos de onda próximos do infravermelho. Tal pode ser altamente interessante, por exemplo, em elétrodos intermédios em arquiteturas de células solares de multi-junção e multi-terminais.

Palavras-chave: Elétrodo condutor transparente, Litografia coloidal, Langmuir-Blodgett, Auto assemblagem, camada anti refletora

Abbreviations

AFM – Atomic Force Microscopy
ARC – Antireflection Coating
AZO – Aluminium zinc oxide
CL – Colloidal lithography
CNT – Carbon nanotube
EDS – Energy Dispersive Spectroscopy
EtOH – Ethanol
FOM – Figure of merit
IPA – 2-propanol
IR – Infrared
ITO – Indium tin oxide
IZO – Indium zinc oxide
LB – Langmuir-Blodgett
MPP – Maximum power point
NIR – Near infrared
NW – Nanowire
OLED – Organic light emitting diode
RIE – Reactive Ion Etching
Rt – Reflectance
SEM – Scanning Electron Microscopy
SiN_x – Silicon nitride
TCE – Transparent conductive electre
TCO – Transparent Conducting Oxide
Tt – Total transmittance
UV – Ultraviolet
UV-VIS-NIR – Ultraviolet-Visible-Nearinfrared

Symbols

cm – Centimeter

η – Efficiency

μL – Microliter

μm – Micrometer

mL – Milliliter

mm –Millimeter

mtorr – Militorr

Ω – Ohm

R_s – Sheet resistance

s – Second

Sccm – Standard cubic centimeter per minute

V – Voltage

n – number of carriers

W – Watt

Table of Contents

List of Figures

List of Tables

Motivation and Objectives

With increasing demand in high-performance transparent conductive electrodes, and with ITO reaching fundamental optical and electrical limits, new materials and techniques must be investigated to produce high-performance optoelectronic devices [1]. This work aims to produce a transparent contact to be applied in solar cells that can compete with ITO, in both optical and electrical properties, while trying to reduce the overall layer thickness (thus lowering the material costs). We set a target of 10 Ω/sq sheet resistance and 80% transmittance (averaged along the main solar spectral range) for a thickness rounding the 70 to 110 nm. For context, 400 nm of ITO deposited at room temperature would be needed to achieve this sheet resistance.

The contacts are fabricated on a glass substrate using an innovative colloidal lithography (CL) technique. This employs polystyrene (PS) microspheres to produce the mask which will allow the creation of the metallic micromesh. Such technique replaces the use of traditional photolithography masks and equipment, resulting in lower costs of production. Furthermore, CL has virtually no limitations in the patterned area, thus allowing high-throughput fabrication, is safe and environmental friendly as the only materials used are PS, ethanol and deionized water.

Ultra-thin (30-40 nm) transparent conductive oxide layers are used both on top and below the micromesh to reduce reflection and passivate the metal against environmental degradation.

Work strategy

This work focused on controlling various fabrication processes whose experimental parameters affect the quality and reproducibility of the resulting transparent electrodes. The main processes optimized here were:

1. Langmuir-Blodgett – Improving the quality of the deposition of the colloidal PS microspheres starts by optimizing the surface tension, allowing the formation of a monolayer of spheres on the water surface, plus the volume and concentration of sphere solution needed to sustain the surface tension value throughout the deposition. In a first stage, only one sphere size solution was used but by the end of this work three different sphere sizes were analysed.

2. Reactive ion etching (RIE) – RIE was used to shape the deposited PS colloids, in order to tune their inter-particle distance. To establish good etching times, power and pressure values were tested based on previous studies conducted at CEMOP [2], and various times were used. The preferential set of etching conditions is the one that consistently allows the formation of a continuous metal mesh in between eroded spheres. Times higher than this are used to study the variation in optical and electrical properties of the samples.

3. Metal used and thickness – Aluminium and silver micromeshes were compared to find a good compromise between optical and electrical properties. After settling for one metal, different thickness values were evaluated, again to find a good compromise between electrical and optical properties.

4. Transparent conductive oxide (TCO) – AZO and IZO layers were tested to coat the micromesh on the rear and front, checking the impact of the differences on complete electrodes. AZO is much lower cost, making it an interesting alternative.

5. The optical and electrical properties of the samples were characterized by UV-VIS-NIR spectrophotometer and hall-effect, respectively. The morphology of the different structures

was characterized by scanning electron microscopy (SEM) and atomic force microscopy (AFM).

Chapter I: Introduction

1.1. Transparent conductive electrodes

Top contact electrodes are of extreme importance for high performance optoelectronic devices such as thin film solar cells, organic light emitting diodes (OLEDs) and display panels. To maximize their efficiency, these electrodes must display characteristics such as high broadband transmittance and electrical conductivity [3–6].

Presently, the preferred material used to fabricate these transparent conductive electrodes (TCEs) is indium tin oxide (ITO), but ITOs optimization has reached fundamental limits. There are also problems concerning ITOs usage as the TCE, as indium is a rare metal and suffers from large price fluctuations that make it undesirable for commercial applications. Furthermore, ITO presents major drawbacks such as a strong absorption in the near ultraviolet (near-UV) and infrared (IR) spectral range and brittleness, which make it unsuitable for flexible substrate applications. The deposition process also poses some issues, as ITO is commercially deposited by dc-magnetron sputtering at high temperatures, which is costly and prevents the use in temperature-sensitive substrates (e.g. most flexible materials) due to the elevated temperatures required for a good quality deposition [1, 3, 4, 6, 7, 8–10].

Currently, there are plenty of materials and geometries being investigated for TCEs, such as macroscopic metallic grids, nanoimprinting, solution-based random metal nanowires (NWs), carbon nanotubes (CNTs) and metal nano/micro-meshes fabricated by various lithography processes. CNTs and metal NWs are two promising candidates to replace ITO as top electrode, with metal NWs having an advantage over the CNTs because of the higher conductivity the metal has to offer [3, 7, 11].

Different methods are used to produce metal NWs such as chemical synthesis, electrospinning, lithographic processes and nanoimprinting. Random silver (Ag) NWs produced by solution-based synthesis have shown better optical and electrical properties compared to ITO films, but the use of silver still carries the cost problem since silver prices are comparable to indium prices. The need to decrease prices lead to research with copper (Cu) NWs. This metal is less expensive than silver or indium, being around 100 times cheaper and about 1000 times more abundant [3, 7, 11, 12]. Printable Cu NWs have shown optical and electrical properties comparable to ITO, but these structures pose some problems. High aspect ratio NWs are needed to maintain high transmittance and, to achieve this, sophisticated solution processes/processing methods must be used. In addition, the density of the NWs must be above the percolation threshold to form a low resistance pathway and, at the same time, be as low as possible as to minimize the reflectance due to the metal. This compromise between electrical and optical properties is proving especially difficult to achieve for Cu NWs, which have high contact resistance between NWs and are easily oxidized.[3, 12]

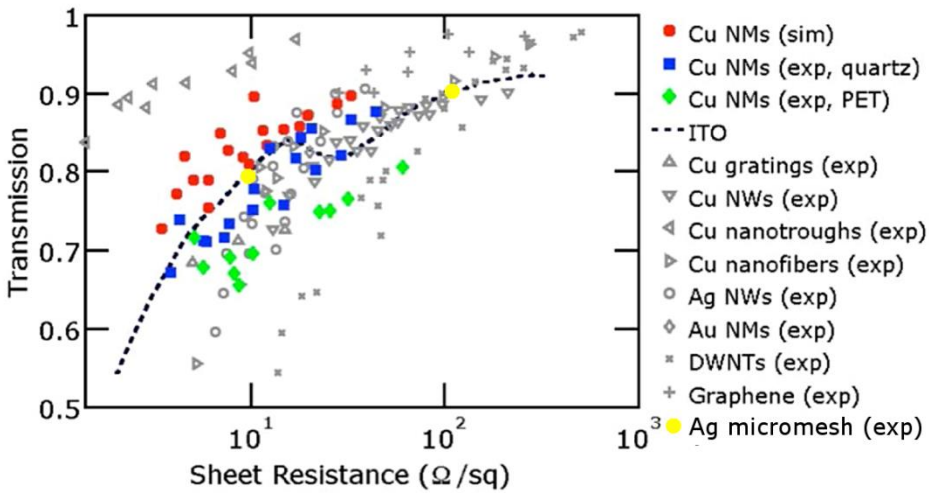

Figure 1 Graph of transmission vs sheet resistance of different methods for fabricating TCEs. Transmission values do not include losses due to substrate. Figure adapted from [3].

The market for TCEs has been increasing over the years, especially for ITO alternatives due to the reasons mentioned previously. In Figure 2, future market predictions for 2016 for ITO in current existing applications and ITO alternatives for emerging applications are shown. ITO is predicted to remain the dominant TCE. However, upcoming applications demand ITO alternatives at a much higher rate than currently existing applications. The market for ITO alternatives for upcoming applications is predicted to sharply increase, representing around 40% of the total market [13].

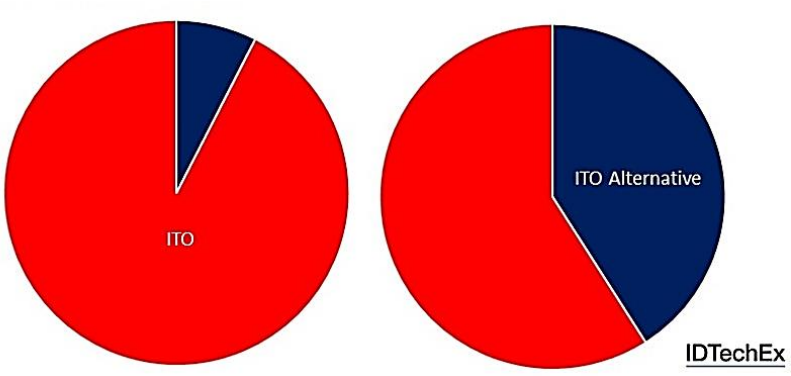

Figure 2. Share of ITO and ITO alternatives in the current existing applications (left) by 2016 and in upcoming applications by 2026 (right). Figure adapted from [13].

1.2. Colloidal lithography

A recent method used to produce similar structures to Cu NWs is self-assembled colloidal lithography (CL). This is a low-cost, fast and scalable method that uses a monolayer of colloidal particles as a mask for subsequent material patterning. This is used in an analogous way to lift-off lithography where the particles act similarly to the photoresist in common lithography processes. The process consists in the four steps represented in Figure 2.

In the first step (Figure 3 a), colloidal suspensions of polystyrene (PS) spheres were used, purchased from Microparticles *GmbH*, with a diameter of 1.3 *μm* and 1.6 *μ*m dispersed in a mixture of water and ethanol (1:3) solutions at a concentration of 2.5% wt. A monolayer of such microspheres is directly deposited on the surface of the substrate following a Langmuir-Blodgett (LB) wet-coating methodology [2]. This process started by depositing a colloidal suspension in the interface between

water and air, using a syringe. The barriers of the LB system are then closed at a controlled speed, driving the floating spheres to self-assemble at such interface in an ordered close-packed hexagonal array. Afterwards, the obtained monolayer is transferred to the surface of the prepared samples by dip coating, with controlled withdrawal speed (see Figure 3 a). Although the deposition occurs relatively fast, one critical condition must be met for the deposition to be successful. This technique is very sensitive to surface tension variations and any contamination in the water can lead to undesirable results.

In the second step (Figure 3 b) after the deposition, the spheres are eroded using reactive ion etching (RIE) and openings are formed in between them. This will allow us to deposit a conductive material, typically a metal, around the spheres (step three - see Figure 3 c). After the removal of the spheres by an ultra-sonic bath in toluene, the thin metal micromesh is created (step four - see Figure 3 d). The morphology of the resulting mesh can be much better controlled over large areas and has more uniform electrical properties than random NWs and the holes formed after the removal of the spheres allow for high transmittances [3, 13, 14]. Toluene isn't an environmentally friendly chemical and some tests have been conducted using IPA paralel to this work showing promising results.

The final TCE should have similar properties to the one presented in fig. 4

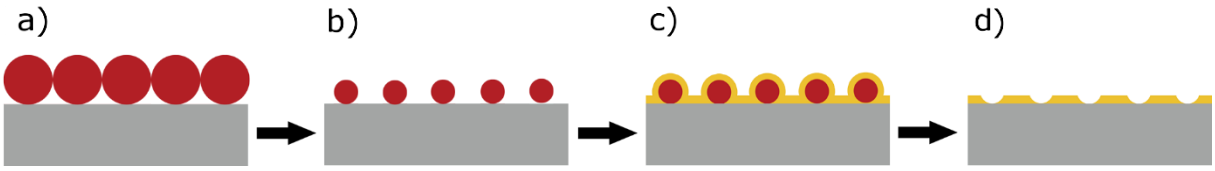

Figure 3 Schematic of colloidal lithography process. a) Close-packed monolayer of colloidal micro-spheres deposited on top of the substrate, forming a regular honeycomb array. b) Non-closed-packed array of spheres formed after dry-etching under O_2 atmosphere. c) A metal film is deposited on top and in between spheres. d) Structured thin metal film resultant from the removal of spheres.

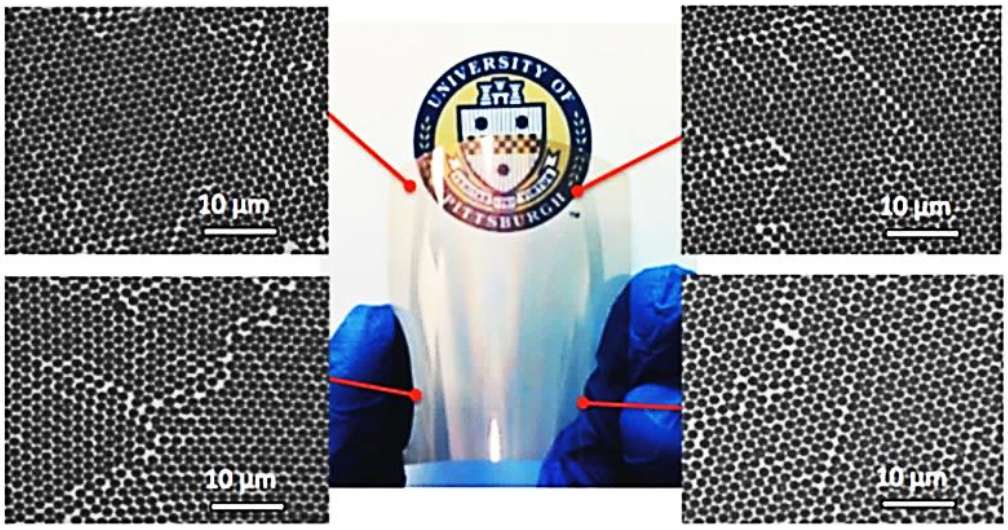

Figure 4 SEM images of samples produced by self-assembly colloidal lithography on a flexible substrate.[3]

This technique has been studied before for this specific application, however, this work shows promising results by using spheres with higher diameters than the visible wavelength. This nullifies the decrease in transmittance caused by the second order plasmon resonance seen in other works [6].

1.3. Effect of metallic materials on the optical properties of the contact

Metallic materials, such as those used for the conductive pathway, tend to produce a strong and undesired reflection of sunlight. However, when structured in nanoscale wires or even wavelength-sized voids, these materials introduce new ways to manipulate light at a subwavelength or wavelength scale [16]. When light hits this structure, the electrons on the material surface oscillate at a certain frequency, driven by the incident electric field. When the frequency of this field matches the natural oscillating frequency of the free electrons in the metallic structure, a resonance can occur, known as a plasmonic mode. The frequency at which the electrons oscillate depends on the structure size, shape and periodicity; in this case, the hole diameter and array pitch. As light penetrates the material, the wavelengths near the resonance frequency can be strongly absorbed and diffracted. By adjusting the original sphere size and etching times we are able to control this resonance frequency and, therefore, the diffracted wavelengths. This can be useful to increase the total pathway of NIR light inside the active layer of thin film solar cells [3, 13, 16–19].

The metallic mesh is typically incorporated within an antireflection coating (ARC) layer, such as ITO or silicon nitride (SiN_x). The optimal ARC thickness is around 70-80 nm and serves to reduce the reflection occurring in the metal and in its void areas, while also protecting the metal from oxidation [4]. The introduction of a conductive micro-mesh on large area solar cells allows for higher spacing within its typical metal fingers, which are used as the pathway for the photocurrent. This can therefore reduce the undesired effects caused by the presence of such metal fingers (sunlight reflection/shading) which lower the current and cell efficiency [4, 14].

1.4. Effect of top contact resistance

In solar cells, the top transparent contact is usually the main contributor for the series resistance of the devices. This is a parasitic parameter responsible for dissipating power and consequently, lowering the overall efficiency of the cell. As such, with increasing sheet resistance the maximum power point (MPP) decreases and this effect is demonstrated in Figure 5.

When considering that solar cells are low voltage but high DC current generators, we can understand that small resistance variations will translate in significant power losses [20–22].

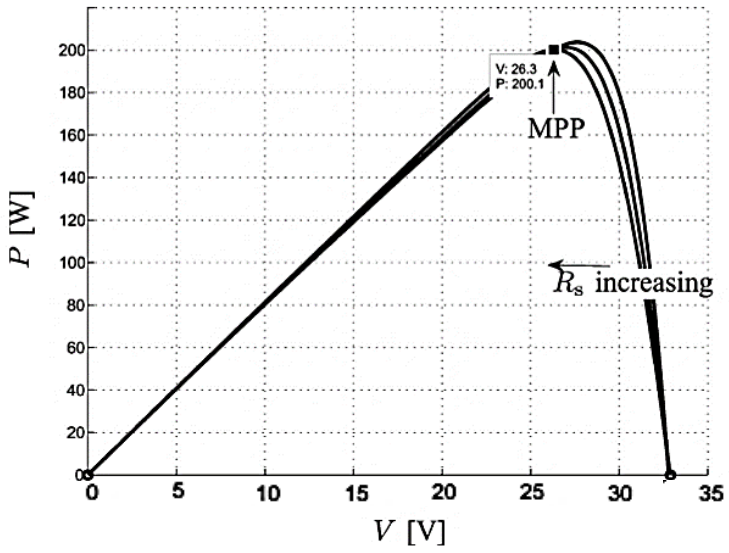

Figure 5 Influence of series resistance on the maximum power point of a solar cell [23].

As stated previously, contacts with higher sheet resistant call for lower spacing within metallic fingers to minimize total sheet resistance, which will increase shading, reduce incident radiation and therefore, lower power generated. An optimal finger spacing can be calculated to reduce overall power losses by considering individual losses due to shading, series resistance and finger resistance. However, lowering such losses should begin by improving the illuminated top contact. In this work, we will evaluate our contacts according to the figure of merit (FOM) calculated using the equation 1, where T is the mean transmittance within a certain wavelength range and R_{sh} is the contact sheet resistance [20–22].

$$FOM = \frac{T^{10}}{R_{sh}} \qquad \text{Equation 1}$$

Note that the transmittance is highly valued (elevated to the power of 10) due to how critical optical losses are to the cell efficiency. Optical properties will determine how much current the cell can generate, meaning that the maximum power generated by a cell is highly dependent on the transmittance through the contact. Another reason for valuing the transmittance so highly relative to the sheet resistance is the fact that optical losses cannot be recuperated. Although the sheet resistance can have a significant impact on the cell efficiency, its effects can be minimized, for example, by using fingers.

1.5. Shading effect on solar cells

Solar cell arrays are composed by individual cells connected in series and/or parallel to meet the intended voltage and current. In solar cell modules, different outputs are bound to exist from one series to another. This is called mismatch and it is a major cause for power losses, as the overall module power output is dependent on the worst performing series. There are a few causes for this mismatch, with partial shading being the most important one. When the module, or even a single solar cell, is partly shaded some of its cells become reverse biased and act as loads, as opposed to power generators. The cells acting as loads will dissipate power generated by nonshaded cells and will drastically reduce the module power output. In extreme cases, the power dissipated by a shadowed cell can be so high or so localized that the cell reaches its thermal breakdown point. In this case, the cell becomes irreversibly damaged in a phenomenon designated as hot-spot [23–27].

Concerning the structures produced in this work, shading effects are reduced by optimizing the silver micro-mesh. This optimization is done by obtaining a good sphere deposition, forming a honeycomb structure and therefore, reducing shading from excessive silver.

Chapter II: Experimental

2.1. TCE fabrication

Various procedures were used due to different variables being studied at distinct stages of this work. This means that the following procedure gives a good description of the method used to produce some of the samples with the best results but does not completely reflect all batches of samples prepared.

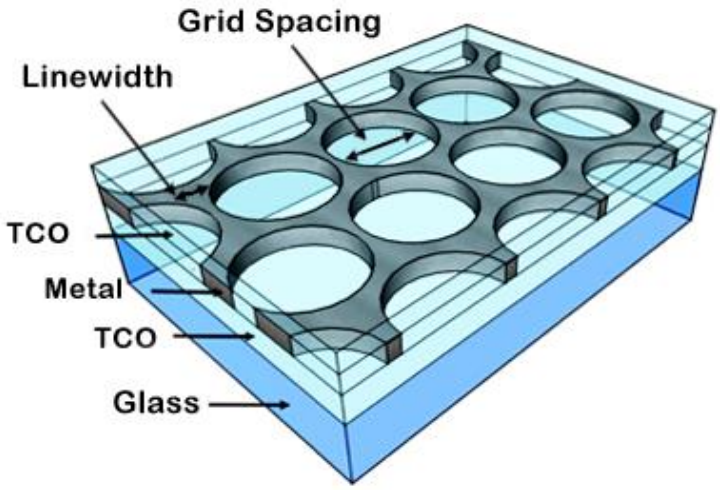

Figure 6 Depiction of a transparent conductive electrode (TCE) produced by colloidal lithography in this work.

2.1.1. Glass preparation

Glass was cut into squares of 2.5 cm × 2.5 cm, rubbed with detergent and cleaned using 10 minutes sonication in acetone, 10 minutes in IPA and 10 minutes in deionized water. The substrates were then dried using a flow of compressed nitrogen.

2.1.2. TCO deposition

Both IZO and AZO were studied, with IZO performing slightly better and due to easier access to the deposition equipment, IZO was chosen for all other depositions.

The glass squares were loaded onto the 3-target system and secondary vacuum was produced. The initial pressure must be lower than 5×10^{-6} mbar to minimize contamination. A partial pressure of 1×10^{-5} mbar of O_2 and 1.5×10^{-3} mbar of Ar was set, and the plasma power was set to 50 W. Before the deposition, we waited 15 minutes for pre-sputtering, followed by 12 minutes of sputtering to grow 30 nm of IZO.

2.1.3. Langmuir-Blodgett

Using the KSV NIMA equipment, various sizes of colloidal spheres were used but the overall procedure is the same. The differences in the procedure refer to volume of solution and surface tension values used.

After making sure that the surface tension is stable at 0 value, this can be achieved by vacuuming impurities, the substrates were lowered, maximum two at a time, and stopping and starting positions were set.

A solution of 600 μL of polystyrene (PS) spheres diluted in ethanol is prepared maintaining a concentration of 25 μg/mL and added slowly to the water surface of the Langmuir-Blodgett using a syringe.

Using the software KSV NIMA we set the surface tension value at which the deposition will take place and the barrier speed to reach said value and start the process. For 1.6 μm spheres the surface tension set was 19 mN/mm. Once the surface tension value set is reached, a new tab is opened, and we set the speed at which the dipper is raised and start the deposition on the substrate(s). In the end a closely packed monolayer of PS spheres should be obtained.

2.1.4. Dry etching

To shape the deposited array of colloidal spheres and form a non-close-packed mask, each sample was etched individually using a Minilock – Phantom RIE ICP in 250 mtorr of O_2 with 20 sccm of O_2 flow and a plasma produced with 90 W. The etching times varied but the most commonly used were 90 s, 120 s, 150 s and 180 s.

2.1.5. Metal deposition

Both aluminum and silver were tested for the conductive electrodes, with silver being the most used throughout the work since aluminum does not come close to achieve the targeted goals.

To deposit silver, the samples are loaded in the E-Beam chamber and secondary vacuum is produced. Once the pressure reaches values below 5×10^{-6} mbar the silver is evaporated with an electron beam and once a good rate is achieved (0.3nm/s to 0.4 nm/s) the shutter is opened and the deposition starts.

2.1.6. Sphere removal (Lift off)

After the deposition of metal and before the final deposition of TCO the spheres must be removed. The samples are submitted to an ultrasonic bath in a toluene recipient for 30 min.

2.1.7. Second TCO deposition

A final layer of TCO is deposited, to finalize the ARC layer and encapsulate the metallic material, using the same procedure employed in the first deposition (section 1.2). In the end, a silver micromesh is formed covered by two layers of 30 nm of IZO each.

2.2. Characterization

2.2.1. UV-Vis Spectrophotometry

The optical characterization of the contacts was based on total transmittance (Tt) and reflectance (Rt) acquired by a Spectrometer UV-Vis-NIR - Perkin Elmer Lambda 950 equipped with an integrating sphere.

2.2.2. SEM-EDS

The morphology of the complete contacts was examined by scanning electron microscopy (SEM) using a Carl Zeiss Auriga crossbeam (SEM-FIB) workstation instrument equipped with an Oxford X-ray energy dispersive spectrometer, and with a Tabletop Microscope TM3030 Plus + Quantax 70 SEM.

2.2.3. AFM

The surface topography of the contacts was also analyzed by atomic force microscopy (AFM, Asylum MFP3D) to analyze contamination observed in SEM images and more accurately measure silver thickness.

2.2.4. Hall-effect

The electrical properties of the contacts, sheet resistance, mobility and number of carriers were measured using the Hall effect - BioRad HL5500 equipment.

Chapter III: Results and Discussion

In this chapter we discuss the optimization of the different variables involved in the fabrication processes, such as colloidal sphere size, etching time, metal used and metal thickness, as well as their influence in the optical and electrical quality of the final metallic nanostructured electrodes.

In the appendices we provide detailed descriptions of the initial test depositions that were performed before attaining the desired etching times, etching pressures and toluene bath times.

3.1. Sphere sizes and reproducibility

In a first stage we compared two different colloidal PS sphere diameters, 1.3 μm and 1.6 μm. Both sphere sizes were compared based on the quality of deposition (good formation of a monolayer with honeycomb structures over large areas) and optical and electrical properties of the micro-mesh structures obtained by using them as lithography mask. To do so, we fixed the rest of the experimental parameters: TCO layer thicknesses, etching time. We used two different silver thicknesses for each sphere size. Samples are labeled according to the metal used and thickness of such metal and according to the sphere size used to produce the mask for the micro mesh. These conditions are summarized in table 1.

Table 1: First batch of targeted sample properties to study sphere size influence on the optical and electrical properties.

Sample	*Bottom IZO thickness (nm)*	*Sphere diameter (μm)*	*Ag thickness (nm)*	*Top IZO thickness (nm)*
Ag_20nm_1.3μm	40	1.3	20	30
Ag_40nm_1.3μm	40	1.3	40	30
Ag_20nm_1.6μm	40	1.6	20	30
Ag_40nm_1.6μm	40	1.6	40	30

Figure 7 shows SEM images of the top view of the different samples analyzed. Their respective total transmittance and reflectance spectra are plotted in the curves of Figure 8.

As can be seen in Figure 7, the 1.6 μm spheres were well deposited forming a honeycomb structure which allows higher transmittance. On the other hand, 1.3 μm spheres were poorly deposited, with more non-uniformities in the array, which resulted in worse transmittance values. Still, we can observe the plasmon resonance for both spheres as the transmittance values drops near the wavelength correspondent to the hole diameter. This dip occurs because the resonant light is being mainly absorbed in the contacts, revealing that the absorption cross section associated to such resonance dominates over the scattering cross section. Therefore, it is preferable to use sphere sizes above the wavelengths of interest for each application. Those used in this work (>1.3 μm diameter) would be suited, for instance, for silicon-based solar cells (or any other PV material with higher bandgap), since these cells can only generate photocurrent for wavelengths up to 1100-1200 nm.

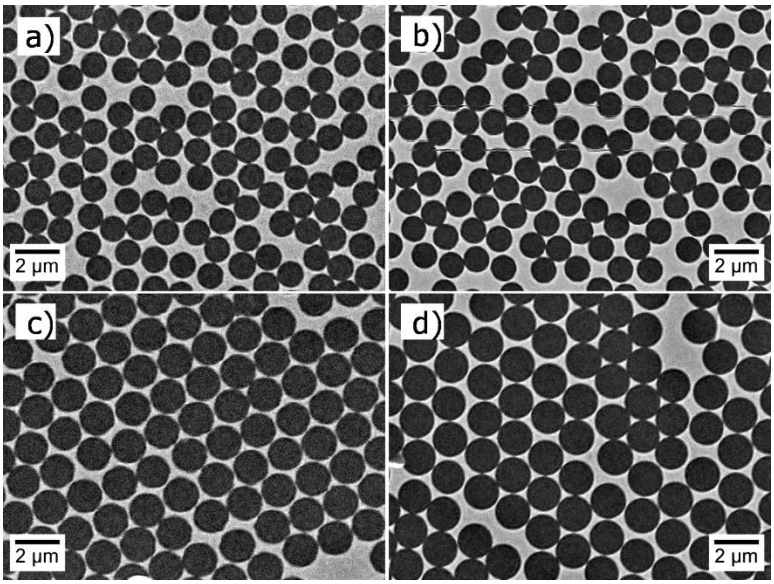

Figure 7 SEM image of the samples prepared using 1.3 µm and 1.6 µm spheres and varied silver thickness. a) sample fabricated with 1.3 µm spheres and 20 nm of silver. b) sample fabricated with 1.3 µm spheres and 40 nm of silver. c) sample fabricated with 1.6 µm spheres and 20 nm of silver. d) sample fabricated with 1.6 µm spheres and 40 nm of silver.

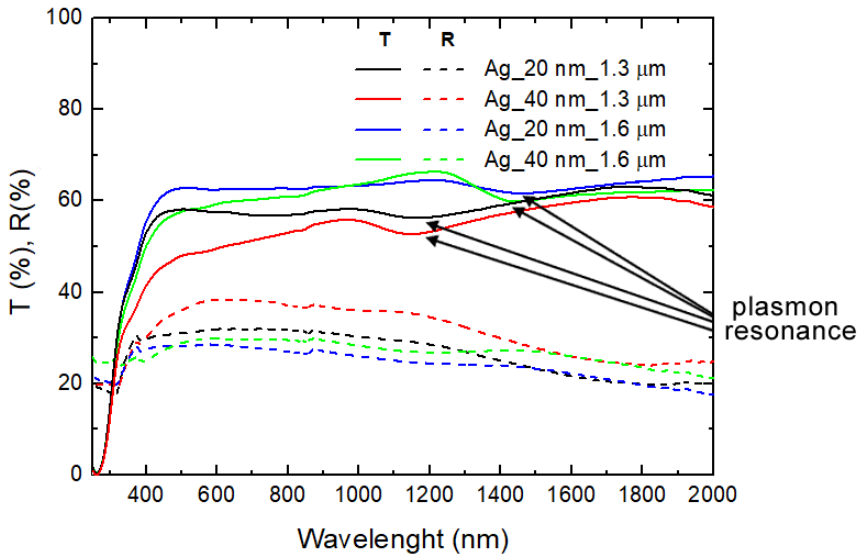

Figure 8 Spectrophotometer results for the samples produced with both 1.3 µm and 1.6 µm spheres and either 20 or 40 nm of silver thickness.

To better evaluate the spheres, we prepared a second batch of samples to try to get a better deposition with 1.3 µm spheres and compared with a sample having a flat silver film against samples with structured silver.

Table 2: Second batch of targeted sample properties to study sphere size influence on the electrical and optical properties of the resulting micro-mesh electrodes.

Sample	*Bottom IZO thickness (nm)*	*Sphere diameter (μm)*	*Ag thickness (nm)*	*Top IZO thickness (nm)*
Ag_30nm_Flat	40	-	30	30
Ag_30nm_1.3μm	40	1.3	30	30
Ag_30nm_1.6μm	40	1.6	30	30

As can be seen in Figure 9, the deposition of 1.6 μm spheres was, once again, much better than the deposition of 1.3 μm spheres, showing a much clear honeycomb structure and a better micromesh coverage overall.

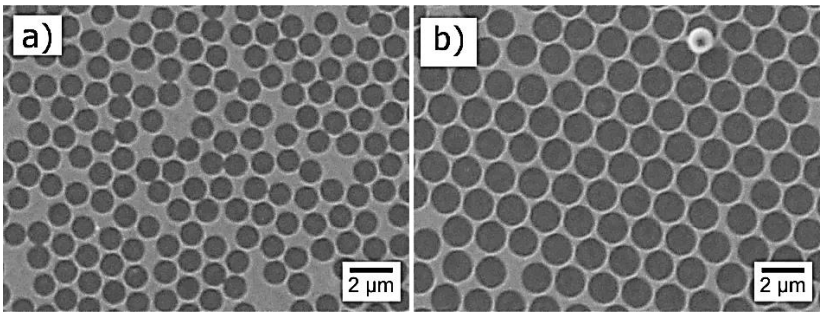

Figure 9 SEM image of the samples prepared using 1.3 μm (a) and 1.6 μm (b) sphere, and 30 nm of silver

Analyzing the spectrophotometer results shown in Figure 10 we can see that the optical properties of samples produced with 1.6 μm spheres are better than samples produced with 1.3 μm spheres at almost all wavelengths. Samples produced with 1.6 μm lose to 1.3 μm in transmittance for wavelengths close to 1.5 μm which is due to the plasmon resonance of the structure produced with 1.6 μm spheres. Both structures have similar transmittance for wavelengths higher than 1.6 μm. As expected, both samples with structured silver showed much better optical results than the sample with a flat silver film.

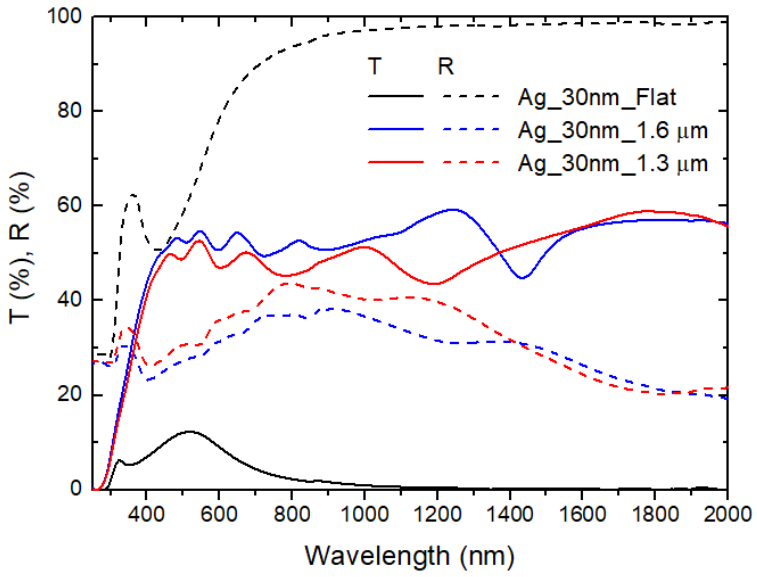

Figure 10 Spectrophotometer results for the 30 nm silver thick samples produced without spheres and with both 1.3 μm spheres and 1.6 μm spheres. Flat 30 nm silver film is represented in black, micromesh produced with 1.6 and 1.3 μm spheres are represented in blue and red respectively. Dash lines represent reflection of each sample.

Table 3: Electrical properties obtained for samples with 30 nm of silver thickness and different sphere sizes. The quantities are defined in section 2.4.

Sample	*Rsh (Ω/sq)*	*μ (cm_2/V-s)*	*n (10^{17}/cm2)*
Ag_30nm_Flat	0.57	20.7	5.23
Ag_30nm_1.6 μm	4.8	4.21	3.11
Ag_30nm_1.3 μm	4.05	4.55	3.38

The electrical results obtained through Hall-effect (see Table 1 give an advantage to the sample produced with 1.3 μm spheres). These results are to be expected as the sample produced with 1.3 μm spheres has a higher silver coverage than the sample produced with 1.6 μm. Around 42% of the structure fabricated with 1.3 μm spheres is covered with silver, as opposed to 35% estimated for the sample fabricated with 1.6 μm spheres. This was calculated using the Gatan Microscopy Suite Software. The flat sample as much lower sheet resistance than both structured samples, however this cannot be used as it acts like a mirror for all wavelengths.

Table 4: Average structural properties of samples with 30 nm silver thickness. Grid spacing represents the average hole diameter and correlates with the plasmon resonance of such structures, the linewidth represents the average distance between holes and silver area represents the percentage of surface covered in silver.

Sample	*Grid spacing, G (μm)*	*Linewidth, W [μm]*	*Silver Coverage (in 100 $μm^2$ area)*
1.3 μm	1.12	0.18	42%
1.6 μm	1.5	0.13	35%

Considering these two batches and previous tests with 1.3 μm spheres we decided that they are not reliable enough to use in further depositions. The structures fabricated with 1.6 μm spheres show better uniformity over large areas, depositions were consistently better, showed better optical behavior until higher wavelengths and showed similar electrical properties to structures fabricated with 1.3 μm spheres despite having much lower area of silver.

3.2. Silver vs Aluminum for the metallic meshes

After choosing the size of colloidal spheres to be deposited we proceeded to test two different metals, silver and aluminum. While silver is a better conductor, aluminum is much more affordable and has higher transparency in the visible range. Two batches of samples were prepared. The first batch consisted of two samples, one being a flat aluminum film (used as reference) and the other being an aluminum micromesh produced using 1.6 μm spheres. The second batch consisted as well of one flat silver film (used as reference) and two samples with silver micromesh. One produced using 1.3 μm spheres and the other using 1.6 μm spheres. All samples had two layers of IZO, a top layer with 30 nm and a bottom layer with 40 nm.

Table 5 summarizes the features of each sample proposed in this section and Figure 11 shows the spectrophotometer results for these samples. Metal thickness variation was due to flawed measurement of aluminum thickness.

Table 5: Targeted sample properties to study the influence of using aluminum (Al) on the electrical and optical properties.

Sample name	*Bottom IZO thickness (nm)*	*Dry Etching time (s)*	*Al thickness (nm)*	*Top IZO thickness (nm)*
Al_35nm_Flat	40	-	35	30
Al_35nm_1.6µm	40	90	35	30

These aluminum samples were compared with the previous 30 nm of silver samples fabricated with 1.6 µm spheres and without spheres.

Taking into account the corresponding spectrophotometer results shown in Figure 11, we can conclude that the optical properties of the aluminum and silver structures are similar. However, analyzing the electrical properties shown in Table 6, we notice a clear difference between silver and aluminum. A flat aluminum film presents roughly the same sheet resistance as a structured silver film, and the sheet resistance of a structured aluminum film is much higher than our targeted value of 10 Ω/sq. In order to improve the electrical properties, we need to sacrifice the optical properties and vice-versa. Considering that aluminum falls short on both, this metal is not the suitable to achieve our goal of 10 Ω/sq and 80% average transmittance.

The silver micromesh shows similar optical properties to the aluminum micromesh and there is still room for improvement by reducing the silver thickness due to the excellent electrical properties.

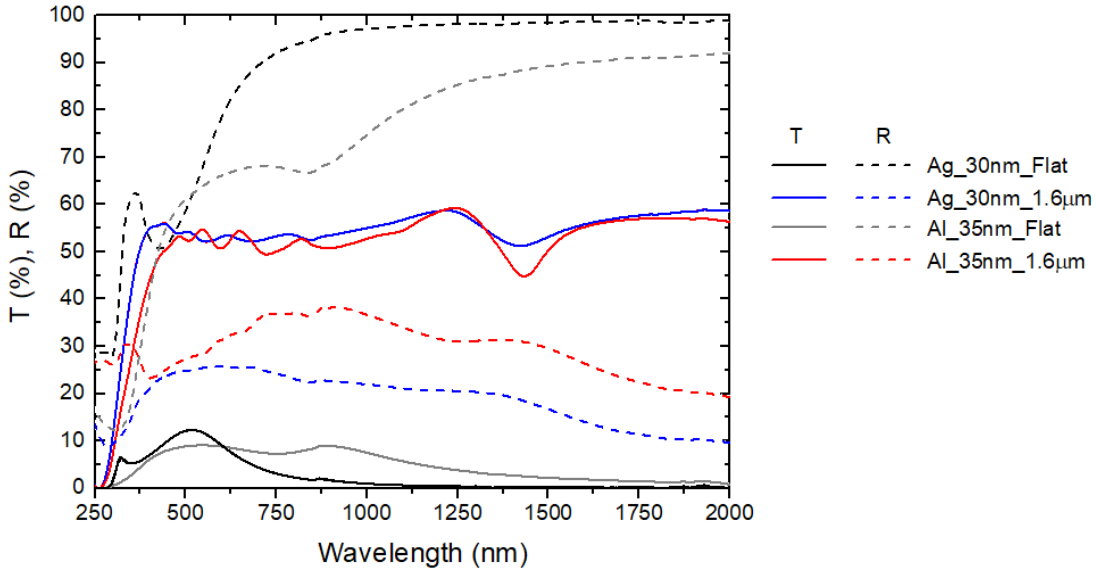

Figure 11 Spectrophotometer results for the 30 nm silver thick samples produced with and without 1.6 µm spheres, blue and black respectively and 35 nm aluminum thick samples produced with and without 1.6 µm spheres, red and gray respectively.

Table 6: Electrical properties of silver and aluminum samples.

Sample	*Rsh (Ω/sq)*	*μ (cm²/V-s)*	*n (10¹⁷/cm²)*
Al_35nm_flat	4.72	3.7	3.57
Al_35_1.6μm	26.3	8.52	0.27
Ag_30nm_flat	0.57	20.7	5.23
Ag_30nm_1.6μm	4.8	4.21	3.11

3.3. Etching time

To reach 80% average transmittance we reduced the silver layer thickness and tested different etching times. By modifying the etching times, we can control the amount of metal (mainly the linewidth, W, see Figure 6, deposited in posterior steps, which enables the study of the influence of W on the optical properties. This should have a noticeable effect on the light transmittance through the silver layer. Samples are labeled according to the metal used and its thickness, mesh structure (flat or structured with a sphere with a certain size) and etching time used when applied.

Table 7: Targeted sample properties to study the etching time influence on the electrical and optical properties.

Sample	*Bottom IZO Thickness (nm)*	*Etching time (s)*	*Top IZO Thickness (nm)*
Ag_10nm_Flat	40	-	30
Ag_10nm_1.6μm_90s	40	90	30
Ag_10nm_1.6μm_120s	40	120	30
Ag_10nm_1.6μm_150s	40	150	30
Ag_10nm_1.6μm_180s	40	180	30

Analyzing the SEM images in Figure 12 we can see that good quality meshes, with a regular array and low defect density, were created for all etching times. The increase in wire width and silver area with etching time is also noticeable, and the approximate values are represented in Table 8.

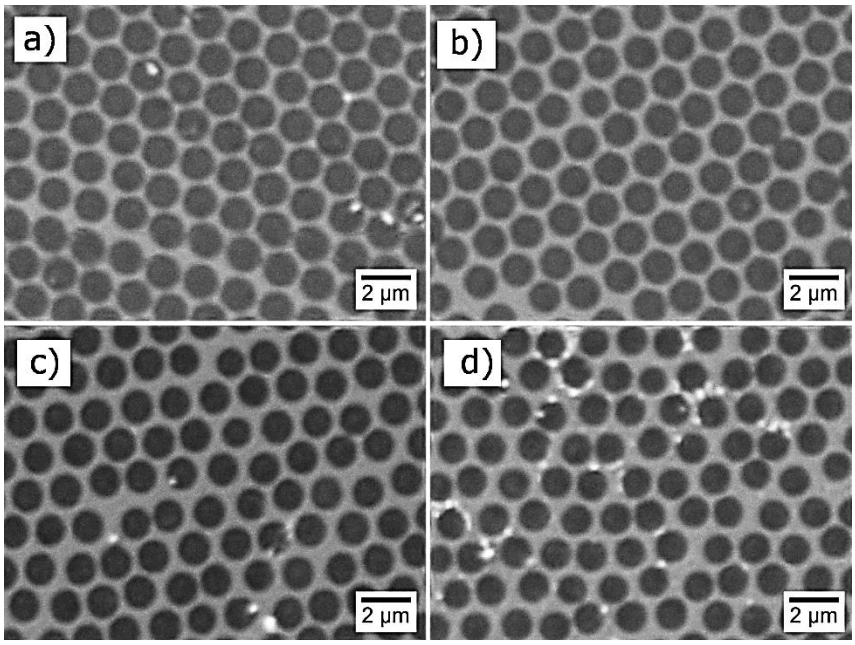

Figure 12 SEM image of the samples prepared using 1.6 µm spheres and varied etching times: a) 90s. b) 120s. c) 150s. d) 180s.

Table 8: Structural properties of the micro-meshes obtained with 10 nm silver thickness and varied etching times.

Sample	*Grid spacing, G (µm)*	*Linewidth, W [µm]*	*Silver Coverage (in 100 µm² area)*
Ag_10nm_1.6µm_90s	1.38	0.20	28 %
Ag_10nm_1.6µm_120s	1.34	0.21	31 %
Ag_10nm_1.6µm_150s	1.26	0.24	40 %
Ag_10nm_1.6µm_180s	1.25	0.35	40 %

Observing the spectrophotometer results shown in Figure 13, we can see that all samples (except the one fabricated with 180 s of etching) reached >70% peak transmittance. The flat film actually shows the highest peak transmittance at around 75-%, but its transmittance drops sharply right after the peak. The structured samples show great transmittance gains relative to the flat Ag film sample in the near infra-red (NIR) region and show a clear correlation between silver area coverage and transmittance in this region. Lower etching times keep the plasmon effect (dip in transmittance in the NIR) to a minimum and allow for better recovery of transmittance at all wavelengths.

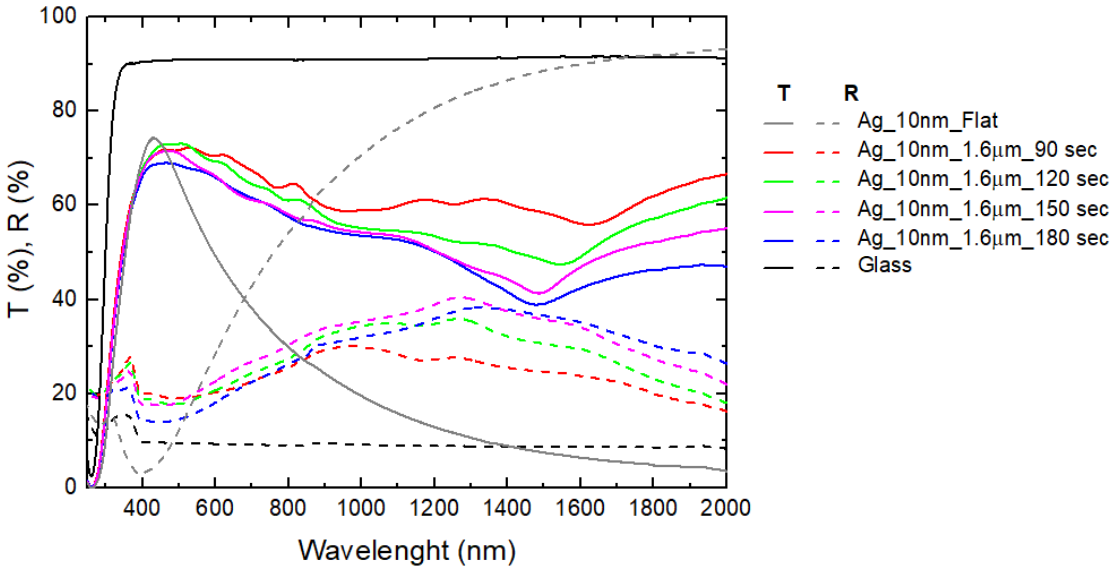

Figure 13 Spectrophotometer results for 10 nm Ag thick samples fabricated with 1.6 µm spheres under varied etching times and a flat (non-structured) 10 nm thick Ag film.

Analyzing the electrical properties shown in Table 9, we can see that two samples, fabricated with 150 s and 180 s of etching, are very close to the targeted 10 Ω/sq. Unexpectedly, the sample fabricated with 180 s of etching shows similar but slightly worse electrical properties than the sample fabricated with 150 s. Both samples were prepared simultaneously at all stages, except for the dry etching process. However, it is possible that some contaminations during the sphere deposition or non-uniform silver deposition during the e-beam process might have worsen the properties of this Ag_10nm_1.6µm_180s sample.

Table 9: Electrical properties of 10 nm silver thick samples with varied etching times.

Sample	*Rsh (Ω/sq)*	*µ (cm^2/V-s)*	*n (10^{17}/cm^2)*
Ag_10nm_Flat	2.64	16.7	14.1
Ag_10nm_1.6µm_90s	26.4	8.08	2.9
Ag_10nm_1.6µm_120s	16.4	6.27	6.1
Ag_10nm_1.6µm_150s	10.6	5	11
Ag_10nm_1.6µm_180s	12.8	3.78	13

Overall, the reduction of metal thickness translated to higher transmittance, as expected. We reached a maximum of 72% and 73 % transmittance for the samples corresponding to 90 s and 120 s of etching, respectively, yielding the highest transmission so far. It is also observed that lower etching times means lower impact of the plasmon effect on the transmittance, translating in a better recovery of transmittance in the NIR region at some expense of the electrical properties. To find the best compromise between electrical and optical properties we used the figure of merit (FOM) given by the equation 1 (shown in Figure 14), where T is the mean transmittance ranging from 300 nm to 1300 nm and R_s is the sheet resistance of the sample.

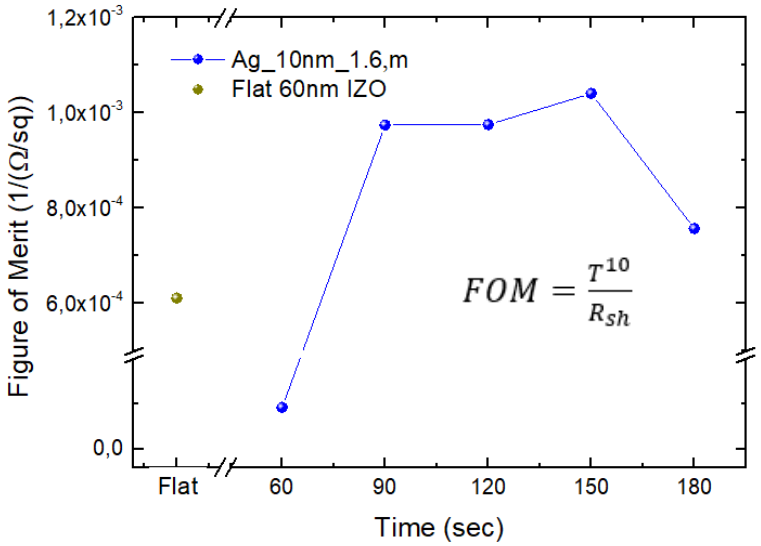

Figure 14 Figure of merit as a function of etching time produced with 10 nm of flat Ag and using 1.6 μm spheres under different etching times. The mean transmittance, T, was calculated between 300 nm and 1300 nm. The FOM for a flat 60 nm IZO (contact thickness without metallic grid) is shown for comparison.

Comparing the different samples based on the figure of merit we conclude that the sample fabricated with 150 seconds of etching shows the best compromise between optical and electrical properties. Samples fabricated with both 90 s and 120 s show similar figure of merit, but their sheet resistance is quite higher than the targeted 10 Ω/sq. The Ag_10nm_1.6μm_150s sample shows a peak transmittance above 71% and 10.6 Ω/sq sheet resistance and considering both IZO layers we should have a 70 nm thick TCE. For comparison, 80 nm of ITO fabricated at room temperature translates in 110 Ω/sq.

3.4. TCO thickness

High losses due to reflection can be observed in the previous spectrophotometer results. In an attempt to reduce these losses, we increased the upper TCO layer thickness to see if the reflectance from the metal could be reduced in favor of the overall transmittance, meaning an enhancement of the ARC structure over the Ag material. Samples are labeled in Table 10 according to the metal, metal thickness and sphere size used (if applied) to produce the micromesh and according to the upper IZO thickness layer. Both structured samples were eroded under 120 s of etching under the same conditions as previous samples (250mtorr O_2 with 20 sccm of O_2 flow and 90 W of RIE power).

Table 10: Targeted sample properties to study TCO thickness influence on the electrical and optical properties.

Sample	*Bottom IZO thickness (nm)*	*Sphere diameter (μm)*	*Ag thickness (nm)*	*Top IZO thickness (nm)*
Ag_10nm_Flat_85nm	30	-	10	85
Ag_10nm_1.6μm_85nm	30	1.6	10	85
Ag_10nm_1.6μm_30nm	30	1.6	10	30

Observing the spectrophotometer results in Figure 15, we can conclude that some reflectance for wavelengths close to 500 nm was reduced, but the reflectance for wavelengths higher than 1300 nm was increased. The reduction in reflectance for wavelengths close to 500 nm did not translate into higher transmittance, suggesting that any possible reduction of reflectance was lost to absorption within the contact.

Overall, the increase in TCO thickness showed only negative results, mainly due to the higher parasitic absorption occurring in the IZO material, except for a small decrease in sheet resistance as can be seen in Table 11.

A sample with only 60 nm of IZO is including in Table 11 to demonstrate the sheet resistance gain by introducing a structured Ag layer. This sample is studied further in appendix D.

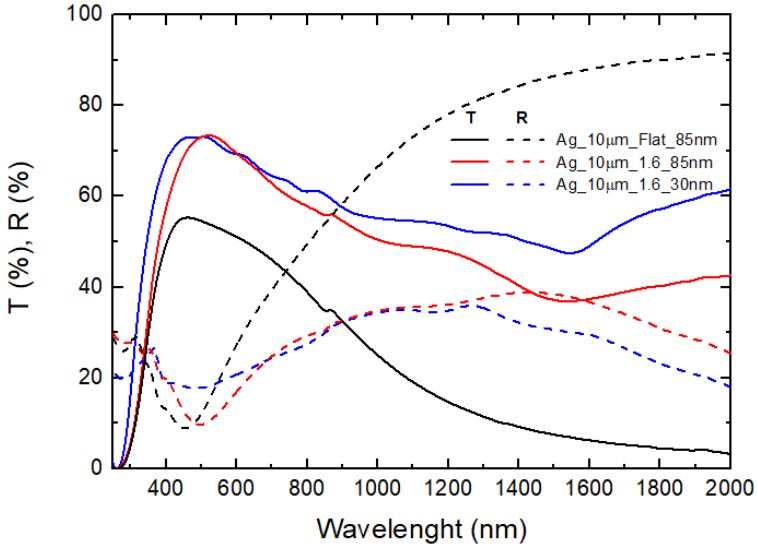

Figure 15. Spectrophotometer results for 10 nm thick samples fabricated with 1.6 µm spheres with different TCO thickness and flat 10 nm film of silver with higher TCO thickness.

Table 11: Electrical properties of 10 nm silver thick samples with varied TCO thickness.

Sample	*Rsh (Ω/sq)*	*µ (cm^2/V-s)*	*n ($10^{17}/cm^2$)*
Ag_10nm_Flat_85 nm	2.64	16.7	14.1
Ag_10nm_1.6µm_85 nm	16	2.13	1.8
Ag_10nm_1.6µm_30 nm	16.4	6.27	6.1
60nm_IZO	252	29.9	0.008

3.5. Different TCO material

As stated previously, minimizing costs is also a point of interest in this work, so we tested AZO against IZO, as aluminum is considerably less expensive than indium. Two identical samples were prepared except for the TCO layers. All stages of fabrication were done simultaneous for both samples with the exception of the deposition of the TCO layers, to allow a better comparison between the samples. Samples are labeled in Table 12 according to the metal, metal thickness and sphere size used (if applied) to produce the micromesh and according to TCO used in both layers. Both structured samples were eroded under 120 s of etching under the same conditions as previous samples (250mtorr O_2 atmosphere with 20 sccm of O_2 flow and 90 W of RIE power).

Table 12: Targeted sample properties to study the influence of the TCO material used on the electrical and optical properties.

Sample	*TCO material*	*TCO thickness (nm)*	*Ag thickness (nm)*
Ag_10nm_Flat_AZO	AZO	30 (2 layers)	10
Ag_10nm_1.6µm_AZO	AZO	30 (2 layers)	10
Ag_10nm_1.6µm_IZO	IZO	30 (2 layers)	10

As can be seen from the spectrophotometer results shown in Figure 16 and electrical results shown in Table 13, the micro-meshed TCE with AZO seems to be worse than the sample with IZO both in optical and electrical properties. Considering that we have not yet achieved the targeted results, sheet resistance barely higher than 10 Ω/sq and peak transmittance around 71 %, it is preferential to use IZO in further depositions.

Taking a closer look to the flat 10 nm sample fabricated with AZO, we notice that the sheet resistance is almost half of the sheet resistance for a flat 10 nm film with IZO. Considering that IZO performed better than AZO in both mobility and density of carriers in the micro-meshed TCEs it would be expected for ITO to outperform AZO in a flat film as well. This can be attributed to an uncertainty in measuring the deposition rate during the silver deposition process, as in these samples any small nanometric variation in silver thickness can provide considerable differences in the sheet resistance. While this can have an effect when comparing samples from different batches, it does not affect samples within the same batch, as the silver is deposited at the same time for all samples.

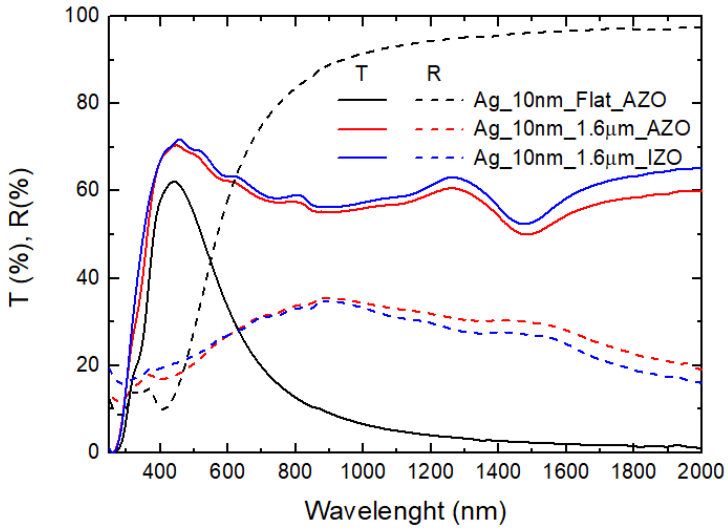

Figure 16. Spectrophotometer results for 10 nm thick samples fabricated with 1.6 µm diameter spheres under 250 mtorr O_2 atmosphere with 20 sccm O_2 flow, 90 W RIE power, 120 s of etching and either IZO or AZO as TCO plus a 10 nm flat film of silver with AZO.

Table 13: Electrical properties of 10 nm silver thick samples with either IZO or AZO as the TCO material.

Sample	*Rsh (Ω/sq)*	*μ (cm^2/V-s)*	*n (10^{17}/cm^2)*
Ag_10nm_Flat_AZO	1.37	22.8	2.0
Ag_10nm_1.6μm_AZO	16	2.13	1.8
Ag_10nm_1.6μm_IZO	13.1	6.02	7.9

3.6. Higher colloidal sphere diameter

In the previous experiments, the use of micro-spheres with size close to the NIR wavelengths induced a plasmon resonance which increased the absorption of radiation (dip in transmittance) at wavelengths close to the spheres' diameter, as such diameter defines the array pitch. This means that the light close to these wavelengths is being absorbed by the contact material, which is an optical loss caused by such resonant effect.

To improve the optical properties in the NIR region, we tested colloidal PS spheres with diameters larger than 2 μm. After trying with four different sizes, two close to 2.5 μm and two close to 5 μm, we chose one of the solutions with spheres having 5 μm diameter. The use of spheres of this size ensures that the plasmon resonance is shifted to much larger wavelengths that fall outside the spectral range of interest for photovoltaics, thus allowing the use of this electrodes for multiple junction cells with multiple terminals [29, 30], in which infrared radiation is of high importance. Samples are labeled in Table 14 according to the metal, metal thickness plus sphere size and etching time used (when applied). In all structured samples, the spheres were eroded under 250mtorr O_2 atmosphere with 20 sccm of O_2 flow and 90 W of RIE power.

Table 14: Targeted sample properties to study the influence of higher sphere sizes on the electrical and optical properties of the TCEs.

Sample	*Top IZO thickness (nm)*	*Sphere diameter (μm)*	*Etching time (s)*	*Bottom IZO Thickness (nm)*
Ag_10nm_Flat	30	-	-	30
Ag_10nm_5μm_120s	30	5.0	120	30
Ag_10nm_5μm_180s	30	5.0	180	30
Ag_10nm_5μm_240s	30	5.0	240	30

From previous SEM images using a SEM Hitachi TM 3030Plus Tabletop we noticed quite a bit of debris on the samples, and spheres that remained after the toluene bath. To better evaluate the structures, we used the SEM-FIB – Zeiss Auriga CrossBeam Workstation which provides better resolution and allows for energy dispersive spectroscopy.

Observing the SEM results for the 10 nm silver samples fabricated with 5 μm and 120 s of etching shown in Figure 17 a) and Figure 17 b) we notice that a very thin silver film is present and quite a bit of debris can be seen inside the holes, suggesting some PS impurities from the spheres remained after the toluene bath. From these images, it is clear this was a bad sphere deposition. In Figure 17 a) we can see that only 5 holes surround the hole on the center of the image instead of 6 and because of this, high linewidth variation follows.

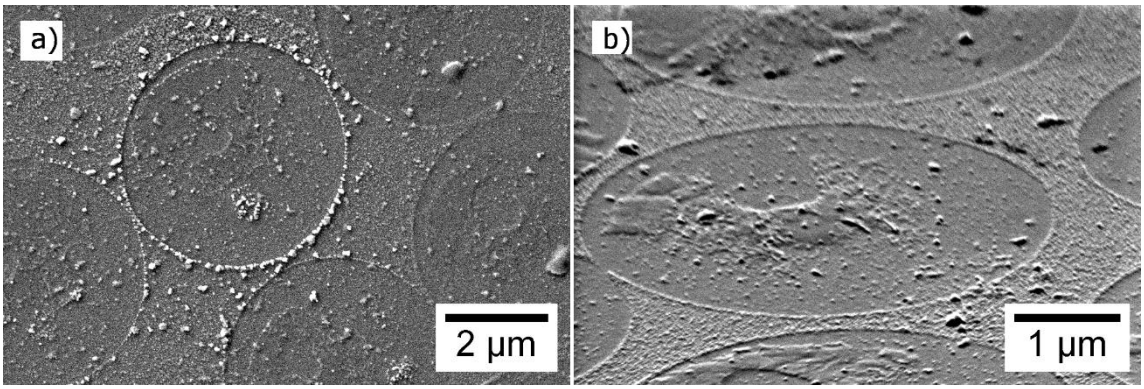

Figure 17 SEM images of the sample fabricated with 5 µm spheres, 10 nm of silver and 120 s of etching. a) Top view of the contact. b) Tilted view with 30 º angle.

During the SEM characterization we used the EDS functionality to obtain more information about the contaminations seen in the SEM images, which were attributed to PS remnants. The characterization was conducted in a hole and on top of the mesh.

As expected, indium, zinc and silver are found in much lower quantity than the other elements. This is due to the small thickness of the contact compared to the glass substrate. The only result that stands out is the amount of carbon present in the sample. It is not unusual to find carbon in EDS characterizations, however it is present in much larger amounts than normal. The most likely explanation for this is the carbon that constitutes the PS spheres.

Comparing results from both spots we notice that a small amount of silver is found in the EDS characterization conducted inside the hole. This can be due to cross contamination during the silver deposition, which will cause a decrease in transmittance through the holes (see appendix C for SEM image of the characterization site and EDS graphs).

Table 15: EDS results conducted inside a hole and on the mesh.

Element	*Hole (atomic %)*	*Mesh (atomic %)*
C	41.65	41.61
O	29.62	27.16
Na	3.53	3.77
Si	19.09	19.01
Zn	0.29	0.32
Ag	0.2	2.28
In	1.56	1.83

To obtain a more precise value for the real silver thickness and to obtain more information on the debris present in the samples, AFM was conducted, and an image of the sample surface can be seen in Figure 18. As expected from previous SEM observations, we found that the thickness of silver present in the sample was much lower than the intended 10 nm, standing at only around 3 nm. The big spikes present in the surface might result from sphere remnants and can have an influence in both optical and electrical properties of the sample. A supposedly PS layer inside the holes can also be seen in Figure 18 and has an average thickness of 10 nm.

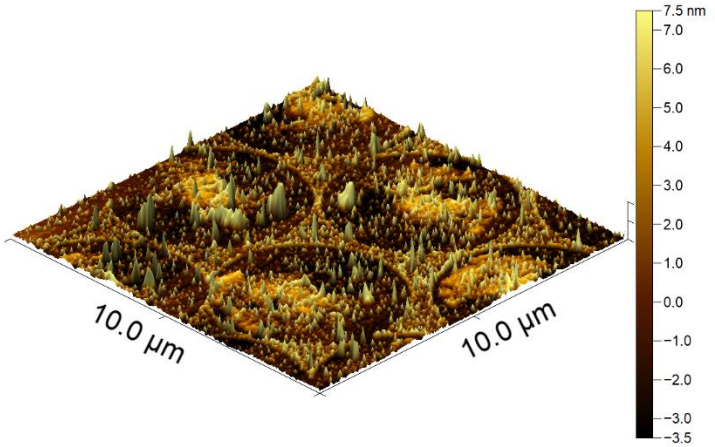

Figure 18 AFM image of the sample fabricated with 5 µm spheres, 10 nm of silver and 120 s of etching

From the AFM results the actual silver thickness was measured, standing at around 4 nm. This is not enough to form a completely uniform film which is why the surface is much rougher than in previous depositions.

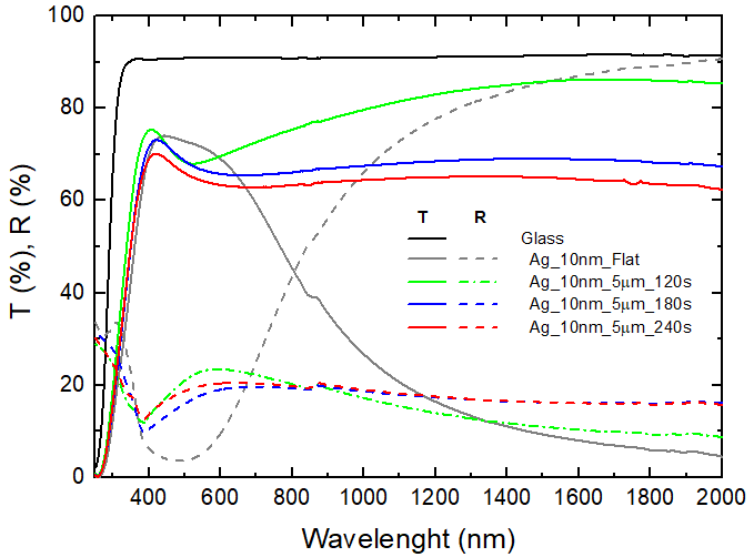

Figure 19Spectrophotometer results for 10 nm thick samples fabricated with 5 µm spheres under varied etching times and a flat 10 nm thick sample.

Considering the very thin silver layer deposited, and the high sphere diameter, high broadband transmittance was expected but bad electrical properties should follow, especially considering the poor quality of sphere deposition.

Table 16: Electrical properties of 10 nm silver thick samples with 5 µm spheres and varied etching times.

Sample	*Rsh (Ω/sq)*	*µ (cm^2/V-s)*	*n (10^{17}/cm^2)*
Ag_10nm_Flat	3.41	12.8	1.43
Ag_10nm_5µm_120s	121	29	0.01
Ag_10nm_5µm_180s	126	30	0.01
Ag_10nm_5µm_240s	134	-	-

These samples presented better optical but worse electrical properties than the previous ones with 1.6 um spheres. The flat silver film sample also presented higher sheet resistance than previous samples which are supposed to have 10 nm of silver. This, again, shows a flaw in the measurement of the silver deposition rate. Possible causes for this are poor calibration of the equipment, low resolution of the deposition rate and the need to manually stop the deposition when closing the shutter.

The silver thickness in this samples was so inconsistent that the increase in etching time did not result in better electrical properties, suggesting that a big percentage of the conduction is being done through the TCO layers as opposed to the silver mesh.

These samples show good optical behavior in the infrared region, however, when considering the electrical properties, it is still preferable to just use ITO as it will present similar qualities with fewer steps.

3.7. Different metal thickness with 5 µm diameter spheres

To circumvent the problem of the poor measurement of silver thickness, we increased the intended thickness to 20 nm and 40 nm. This should also facilitate the study of this spheres size at earlier stages. Samples are labeled in Table 17 according to the metal, metal thickness plus sphere size and etching time used (when applied). The spheres in all structured samples were eroded under 250mtorr O_2 atmosphere with 20 sccm of O_2 flow and 90 W of RIE power.

Table 17: Targeted sample properties to study the influence of silver thickness on the electrical and optical properties when using 5 µm colloidal spheres.

Sample	*Top IZO Thickness (nm)*	*Sphere diameter (µm)*	*Etching time (s)*	*Ag (nm)*	*Bottom IZO thickness (nm)*
Ag_20nm_Flat	30	-	-	20	30
Ag_40nm_Flat	30	-	-	40	30
Ag_20nm_5µm_120s	30	5.0	120	20	30
Ag_40nm_5µm_120s	30	5.0	240	40	30
Ag_20nm_5µm_120s	30	5.0	120	20	30
Ag_40nm_5µm_240s	30	5.0	240	40	30

Observing the SEM images shown in Figure 20 for the 20nm silver thick sample produced with 5 µm spheres and 120 s of etching, we can see that the quality of sphere deposition is slightly better. Due to the short etching time, several wires are cut which will affect the electrical properties, but overall the spheres are arranged much more closely packed.

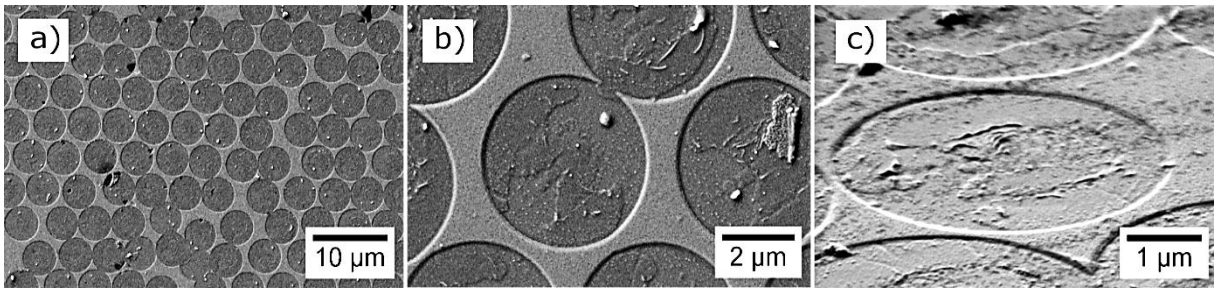

Figure 20 SEM images of the sample fabricated with 5 µm spheres, 20 nm of silver and 240 s of etching. a) Top view of the contact. b) Close up of the top view. c) Tilted view with 30 º angle.

Once again, AFM images were taken for the samples prepared with 120 s of etching. In Figure 21, we can see a much clearer differentiation between silver and holes due to the higher silver thickness. The average silver thickness was 25 nm, being relatively close to the intended 20 nm. The supposed PS contamination is also present in this sample, with some spikes inside the holes and a thinner film, again with around 10 nm of thickness.

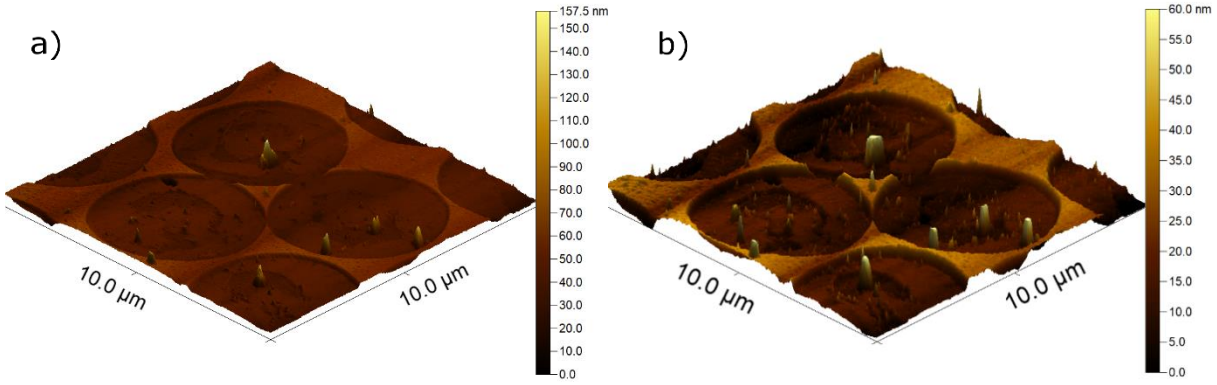

Figure 21: AFM images (with different height, z, scale) of the sample fabricated with 5 µm spheres, 20 nm of silver and 120 s of etching

Analyzing the spectrophotometer results shown in Figure 22, we can see a decrease in transmittance when compared to the previous samples (Figure 22), as expected. These samples show considerably more silver and are still not fully optimized. Nonetheless, the sample produced with 120 s of etching shows an average 65 % transmittance from 300 nm to 2000 nm which shows some potential for use in cells which make use of higher wavelength radiation, such as multi-junction solar cells.

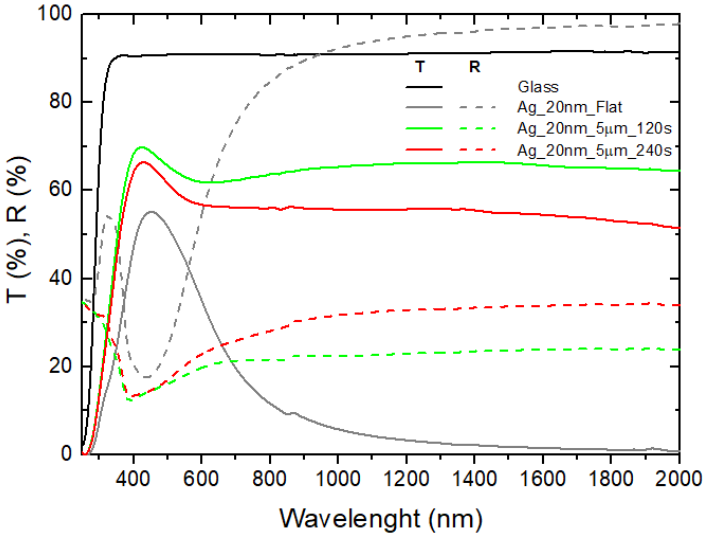

Figure 22 Spectrophotometer results for 20 nm thick samples fabricated with 5 µm spheres under varied etching times and a flat 20 nm thick sample9

When analyzing the SEM images of samples produced with 40 nm of silver we notice a similar good quality of sphere deposition. There are some defects present, such as missing holes, as can be seen in Figure 23 a), and cut silver pathways as can be seen on the bottom left of Figure 23 b).

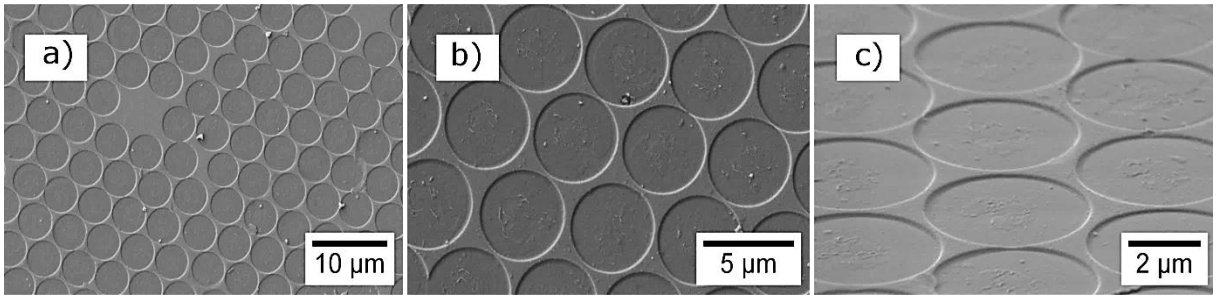

Figure 23. SEM images of the sample fabricated with 5 µm spheres, 40 nm of silver and 120 s of etching. a) Top view of the contact. b) Top view of the contact. with higher magnification c) Tilted view with 30 º angle.

However, the AFM analysis obtained for this sample showed much higher silver thickness than intended, standing at around 75 nm instead of 40 nm. This explains the mirror like properties of the flat silver film seen in Figure 24. Once again, a thin layer with around 10 nm, possibly of PS remnants, was measured inside the holes of these samples.

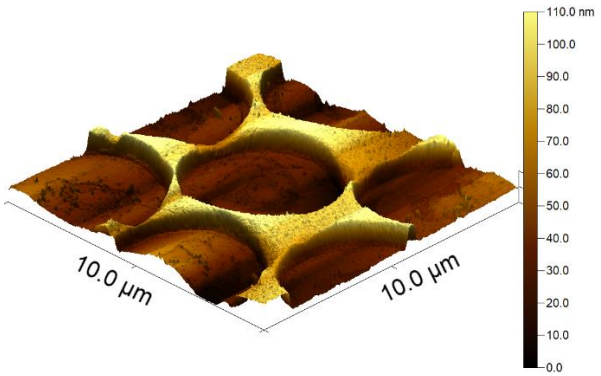

Figure 24. AFM image of the sample fabricated with 5 µm spheres, 40 nm of silver and 120 s of etching

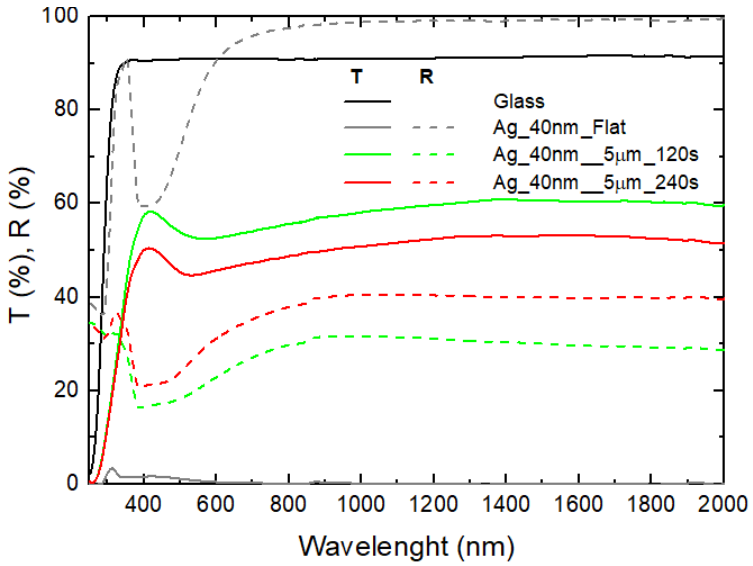

Figure 25 Spectrophotometer results for 40 nm thick samples fabricated with 5 μm spheres under varied etching times and a flat 40 nm thick sample

Table 18: Electrical properties of samples fabricated using 5 μm spheres and varied silver thickness and etching time.

Sample	*Rsh (Ω/sq)*	*μ (cm²/V-s)*	*n (10¹⁷/cm²)*
Ag_20nm_Flat	1.33	24.3	1.93
Ag_20nm_5μm_120s	69.7	21	0.04
Ag_200nm_5μm_240s	22.1	6.63	0.42
Ag_40nm_Flat	0.3	27.3	7.31
Ag_40nm_5μm_120s	18.3	5.87	0.58
Ag_40nm_5μm_240s	6.1	3.89	2.63

Analyzing the electrical results for samples with 20 and 40 nm of silver we can see that only one structured sample (Ag_40nm_5μm_240s) presents sheet resistance lower than the targeted value. These results suggest that the targeted sheet resistance value may not be possible to achieve without sacrificing optical properties. Although some improvements in sphere deposition can be achieved to obtain better optical results, the fact that only the 40 nm silver sample with 240 s of etching broke the targeted value indicates that the main focus for these contacts should be on the transmittance instead of sheet resistance.

Samples produced with 5 μm diameter spheres were compared with previous samples using the figure of merit. The IR range was increased to 2000 nm as these spheres are meant to produce samples with better transmittance at higher ranges. This range can be used for multi-junction solar cells and other optoelectronic devices.

From Figure 26, the sample Ag_10nm_5μm_120s stands out as the top contender for application in solar cells where higher wavelengths in the NIR are of considerable importance, mainly

due to its better transmittance. Considering the lackluster sphere deposition, this sample might achieve better electrical and optical results.

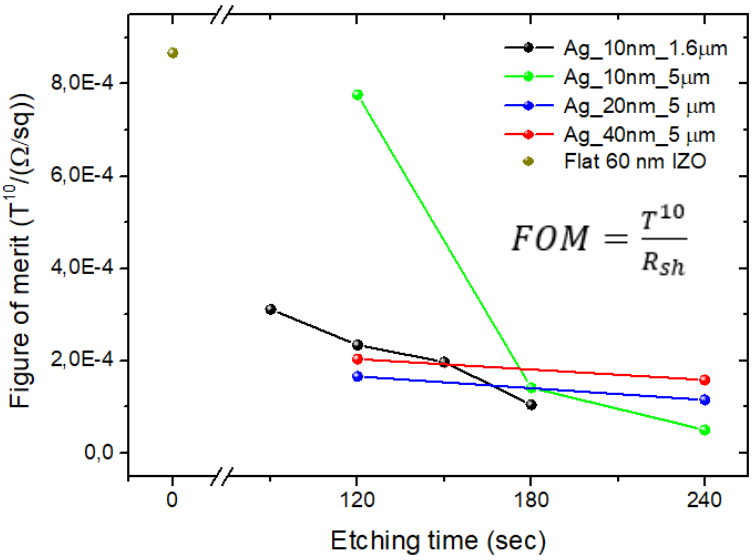

Figure 26. FOM as a function of etching time produced with 10 nm of silver flat and using 1.6 μm spheres and produced with 5 μm spheres with varying silver thickness. The mean transmittance was calculated between 300 nm and 2000 nm. The FOM for a flat 60nm of IZO is also shown – note that its high value is mainly due to better transmittance, but its sheet resistance (252 Ω/sq) is much higher than our target of 10 Ω/sq.

3.8. Attempt to improve contacts

To try to work around the PS contamination we prepared another batch of samples. Four samples were prepared in total. A sample with flat 60 nm of IZO, a sample with flat 15 nm of silver in between two IZO layers 30 nm thick, a sample with 15 nm structured film in between two IZO layers 30 nm thick and a sample with both 15 nm silver film and top 30 nm IZO structured on top of the bottom 30 nm thick IZO layer. The IZO layer was also structured to reduce its absorption and reflection. The samples were meant to be subjected to dry etching after the removal of the spheres, to attempt to etch the PS remnants, however we noticed that this process damaged the sample with structured silver. So, we skipped this stage on the other sample. This process might still be a viable option to remove the PS contamination, however, lower power and lower etching times must be used. Also, different gases and pressures should be tested in the RIE chamber.

Table 19: Electrical results of the different samples prepared

Sample	*Rsh (Ω/sq)*	*μ (cm^2/V-s)*	*n ($10^{17}/cm^2$)*
Ag_15nm_Flat	1.47	24.7	1.79
Ag_15nm_1.6μm_Ag	3230	9.23	0.002
Ag_15nm_1.6μm_Ag/IZO	6.91	6.11	1.48
60nm_IZO	252	29.9	0.008

Chapter IV: Conclusions and Future Trends

Innovative metallic, transparent, nanostructured electrodes were developed using a colloidal lithography method. To achieve our best performing contact, we studied the different experimental variables, going from perfecting the deposition of polystyrene spheres with 1.6 um and studying other sizes to find the best etching parameters. We also studied the behavior of aluminum and silver with different thicknesses and how they translate into optical and electrical properties, and we tested two transparent conductive oxides to obtain the best optical properties within the anti-reflection coating layer.

The most challenging part of this work is to assure a good deposition of PS spheres through the Langmuir-Blodgett method, and this stage proved fatal for spheres with 1.3 μm and so far, for 5 μm spheres as well. In the first part of this work we tested 1.3 μm and 1.6 μm PS spheres, however we were only able to obtain consistent high-quality depositions for spheres with 1.6 μm diameter. Spheres with 1.3 μm showed good optical and electrical properties in some depositions, but they were more unreliable, resulting in low quality depositions most of the time.

The reaction ion etching time was another important variable we investigated during this thesis. First, we established a minimum time which would allow for a continuous mesh to be formed. At earlier stages the time used was 60 s, however we observed in subsequent samples that this time was not enough to consistently produce an unbroken mesh, so the time was then increased to 90 s. The best overall time, 150 s, was extracted from looking at the FOM of different samples. This time should give us the best balance between optical and electrical properties. However, it is of our opinion that the transmittance is valued too greatly (i.e. elevated to the power of 10) in the equation used to obtain the FOM, when the sheet resistance is also of high importance for opto-electronic devices as large-area solar cells. Therefore, the determining evaluation must be performed by applying these contacts in solar cells, to check which would produce the best performing cells.

After settling for a sphere size, we tested aluminum against silver for the mesh material. Aluminum was an interesting choice for the mesh as it is much lower cost than silver, however it simply could not compete with silver as was shown. The optical differences between the two were barely noticeable, but silver was always better in terms of sheet resistance. Unlike with silver, the aluminum sheet resistance and transmittance were already respectively higher and lower than the values we aimed to obtain, 10 Ω/sq and 80% transmittance. This means that we could not reduce aluminum thickness to achieve the 80% as it would increase the sheet resistance, nor could we increase aluminum thickness to achieve 10 Ω/sq as it would decrease transmittance.

The last variable investigated was the material of the TCO layer. We tested IZO and AZO and tested the influence of the thickness of the TCO layer in optical and electrical properties. AZO was an interesting choice for the TCO layer much like aluminum was as a contender for the mesh, as aluminum is much cheaper than indium; but once again, we could not reaching desired results, with IZO showing better optical properties over all radiation ranges. As for the different TCO thicknesses, the little research we conducted proved useless at reducing reflectance losses and even resulted in the opposite effect for higher NIR wavelengths.

When incorporating the best results of all the analyses, (silver, two layers of IZO 30 nm thick , 1.6 μm diameter spheres and 150 s of etching) we obtained a contact with 10.6 Ω/sq, 75 % peak transmittance and 63.7% average transmittance, almost reaching the target we set and achieving the highest FOM for the 300 nm to 1300 nm range (1.04×10^{-3} $(\Omega/sq)^{-1}$).

Additional research with 5 μm spheres was conducted with the intention of shifting the plasmon transmittance dip to irrelevant wavelengths. Using different sphere size means different Langmuir-Blodgett parameters, such as solution volume, sphere to solvent ratio and surface tension used to deposit the spheres. These parameters were not perfected to the same level of the 1.6 μm spheres parameters, which is one cause for the sub-optimal results we see from these samples. Nonetheless, we still achieved high transmittance, peaking at around 85% and averaging at 78,9% for a contact produced with these spheres, although the sheet resistance is much higher than the target value, standing at 126 Ω/sq. This sample did not reach a FOM quite as high as a 60 nm IZO film (7.77×10^{-4} $(\Omega/sq)^{-1}$ for the Ag_10nm_5μm_120s sample and 8.67×10^{-4} $(\Omega/sq)^{-1}$ for the flat IZO film) but presented

half the sheet resistance. If the transmittance is too highly valued in the FOM equation a non-fully optimized Ag_10nm_5μm_120s sample might still be better than a simple flat 60 nm IZO layer.

Both of these structured samples were compared in Figure 1, in yellow, and as can be seen, they are about as efficient as ITO. However, the sample Ag_10nm_1.6μm_150s has a great advantage over ITO as it far thinner. In order to achieve 10 Ω/sq with, we would need a 400 nm thick layer. As was stated in the Introduction, ITO is very brittle and by replacing it for IZO, which is not as brittle, and by fabricating a contact almost 6 times thinner we can increase its resistance to physical stress.

To finalize the work, we tried to optimize the structures by producing one last batch of samples where one had an upper layer of structured IZO and introducing one more dry etching step to remove the PS contamination. Though this batch did not prove to be as successful as we intended, due to the failed dry etching step, we managed to produce another structure that shows some potential for future trials. The sample with structured silver and IZO showed good electrical and optical results despite the low-quality silver mesh.

Future perspectives

In future works, AZO should be considered for more trials as a replacement for IZO in low cost solar cells with high band gap such as perovskite. Even though IZO proved better optically, the differences were not that significant until longer NIR wavelengths where solar power is not as strong. In this work we settled for IZO not only because of the slightly better optical properties but also because of the easier access to the deposition equipment. Given the limited time to complete this thesis, and the fact that IZO does indeed produce higher quality contacts, we focused on using the best materials to achieve the goal set in the beginning. As a result, little research was done using AZO.

Throughout this work we noticed some spheres remained inside the mesh and after SEM and AFM characterization we observed thin films, around 10 nm thick, of PS in every hole of the mesh. Even though the films are very thin, some optical losses are bound to exist. To try and remove all spheres, more time should be used for toluene bath or even find another way to remove said spheres. The thin films can be removed submitting the samples to another dry etching with mild conditions after the toluene bath and before the deposition of IZO.

IPA might be a good alternative to toluene for the removal of PS spheres as it showed comparable results and is much more environmentally friendly than toluene.

References

[1] A. Eshaghi and A. Graeli, “Optik Optical and electrical properties of indium tin oxide (ITO) nanostructured thin films deposited on polycarbonate substrates ‘ thickness effect ,’” *Opt. - Int. J. Light Electron Opt.*, vol. 125, no. 3, pp. 1478–1481, 2014.

[2] O. Sanchez-sobrado *et al.*, “Colloidal-lithographed TiO2 photonic nanostructures for solar cell light trapping,” *J. Mater. Chem. C*, 2017.

[3] T. Gao, B. Wang, B. Ding, J. Lee, and P. W. Leu, “Uniform and Ordered Copper Nanomeshes by Microsphere Lithography for Transparent Electrodes,” 2014.

[4] M. W. Knight, J. Van De Groep, P. C. P. Bronsveld, W. C. Sinke, and A. Polman, “crossmark,” *Nano Energy*, vol. 30, no. July, pp. 398–406, 2016.

[5] J. Krantz *et al.*, “Spray-Coated Silver Nanowires as Top Electrode Layer in Semitransparent P3HT : PCBM-Based Organic Solar Cell Devices,” pp. 1711–1717, 2013.

[6] A. J. Morfa *et al.*, “Transparent metal electrodes from ordered nanosphere arrays Transparent metal electrodes from ordered nanosphere arrays,” vol. 54502, no. 2013, pp. 6–12, 2014.

[7] P. Spinelli and A. Polman, “Transparent Conducting Silver Nanowire Networks,” 2012.

[8] V. Senthilkumar, P. Vickraman, M. Jayachandran, and C. Sanjeeviraja, “Structural and optical properties of indium tin oxide (ITO) thin films with different compositions prepared by electron beam evaporation,” *Vaccum*, vol. 84, no. 6, pp. 864–869, 2010.

[9] G. F. Li, J. Zhou, Y. W. Huang, M. Yang, J. H. Feng, and Q. Zhang, “Indium zinc oxide semiconductor thin fi lms deposited by dc magnetron sputtering at room temperature,” vol. 85, pp. 22–25, 2010.

[10] N. Ito, Y. Sato, P. K. Song, A. Kaijio, K. Inoue, and Y. Shigesato, “Electrical and optical properties of amorphous indium zinc oxide films,” vol. 496, pp. 99–103, 2006.

[11] D. Zhou, Y. Pennec, T. Xu, Y. Lambert, Y. Deblock, and M. Faucher, “applications Optimization of the optical properties of nanostructured silicon surfaces for solar cell applications,” vol. 134304, 2014.

[12] B. A. R. Rathmell, S. M. Bergin, Y. Hua, Z. Li, and B. J. Wiley, “The Growth Mechanism of Copper Nanowires and Their Properties in Flexible , Transparent Conducting Films,” vol. 100190, pp. 3558–3563, 2010.

[13] K. Ghaffarzadeh and R. Das, “Transparent Conductive Films and Materials 2018-2028: Forecasts, Technologies, Players: IDTechEx,” 2018.

[14] M. Retsch *et al.*, “Colloidal self-assembly concepts for light management in photovoltaics,” vol. 18, no. 4, 2015.

[15] J. Zhu *et al.*, “Metallic nanomesh electrodes with controllable optical properties for organic solar cells,” vol. 143109, no. 2012, pp. 10–14, 2013.

[16] M. L. Brongersma, Y. Cui, and S. Fan, “Light management for photovoltaics using high-index nanostructures,” *Nat. Publ. Gr.*, vol. 13, no. 5, pp. 451–460, 2014.

[17] J. Grandidier *et al.*, “pss,” vol. 260, no. 2, pp. 255–260, 2013.

[18] J. Labelle, S. M. Thon, X. Lan, S. Hoogland, M. M. Adachi, and E. H. Sargent, “Broadband solar absorption enhancement via periodic.”

[19] M. J. Mendes *et al.*, “Design of optimized wave-optical spheroidal nanostructures for photonic-enhanced solar cells,” 2016.

[20] X. H. Li *et al.*, “Light trapping in thin-film solar cells via scattering by nanostructured antireflection coatings Light trapping in thin-film solar cells via scattering by nanostructured antireflection coatings,” vol. 44310, 2013.

[21] R. J. Handy, “der Kontaktstrelfen zur Stromaufnahme bedeutet,” vol. 10, pp. 765–775, 1967.

[22] D. Pysch, A. Mette, and S. W. Glunz, “A review and comparison of different methods to determine the series resistance of solar cells,” vol. 91, pp. 1698–1706, 2007.

[23] M. G. Villalva, J. R. Gazoli, and E. R. Filho, “Comprehensive Approach to Modeling and Simulation of Photovoltaic Arrays,” vol. 24, no. 5, pp. 1198–1208, 2009.

[24] T. S. Wurster and M. B. Schubert, “ScienceDirect Mismatch loss in photovoltaic systems,” *Sol. Energy*, vol. 105, pp. 505–511, 2014.

[25] J. Bai, Y. Cao, Y. Hao, Z. Zhang, S. Liu, and F. Cao, “ScienceDirect Characteristic output of PV systems under partial shading or mismatch conditions,” *Sol. Energy*, vol. 112, pp. 41–54, 2015.

[26] S. W. Ko *et al.*, “Electric and thermal characteristics of photovoltaic modules under partial shading and with a damaged bypass diode,” *Energy*, vol. 128, pp. 232–243, 2017.

[27] M. C. Alonso-garcı, J. M. Ruiz, and F. Chenlo, “Experimental study of mismatch and shading effects in the I – V characteristic of a photovoltaic module,” vol. 90, pp. 329–340, 2006.

[28] J. Wohlgemuth and S. International, “BP John Wohlgemuth’li and Werner Herrmann’’) Solar International, Frederick, Maryland,” no. I, pp. 1062–1065.

[29] C. D. Bailie *et al.*, “Semi-transparent perovskite solar cells for tandems with silicon and CIGS,” *Energy Environ. Sci.*, vol. 8, no. 3, pp. 956–963, 2015.

[30] T. Duong *et al.*, “Rubidium Multication Perovskite with Optimized Bandgap for Perovskite-Silicon Tandem with over 26% Efficiency,” *Adv. Energy Mater.*, vol. 7, no. 14, pp. 1–11, 2017.

Appendices

At the start of this work, we aimed to produce meshes with 100 nm linewidth, and to do so we tested different conditions of etching time and pressure based on previous results conducted at CEMOP, RIE power and O_2 flow were fixed at 90 W and 20 sccm respectively.

A. First study of width variation with pressure and etching time

A total of seven samples were produced with 1.3 µm spheres. Four samples were produced under fixed 120 s of etching and varying pressures of 200, 225, 250 e 250 mTorr, and the other three were produced under 250 mTorr and varying times of 90, 150 and 180 s.

From the SEM images in Figure 27 it is clear that an increase in etching pressure leads to a decrease in etching rate of the PS spheres.

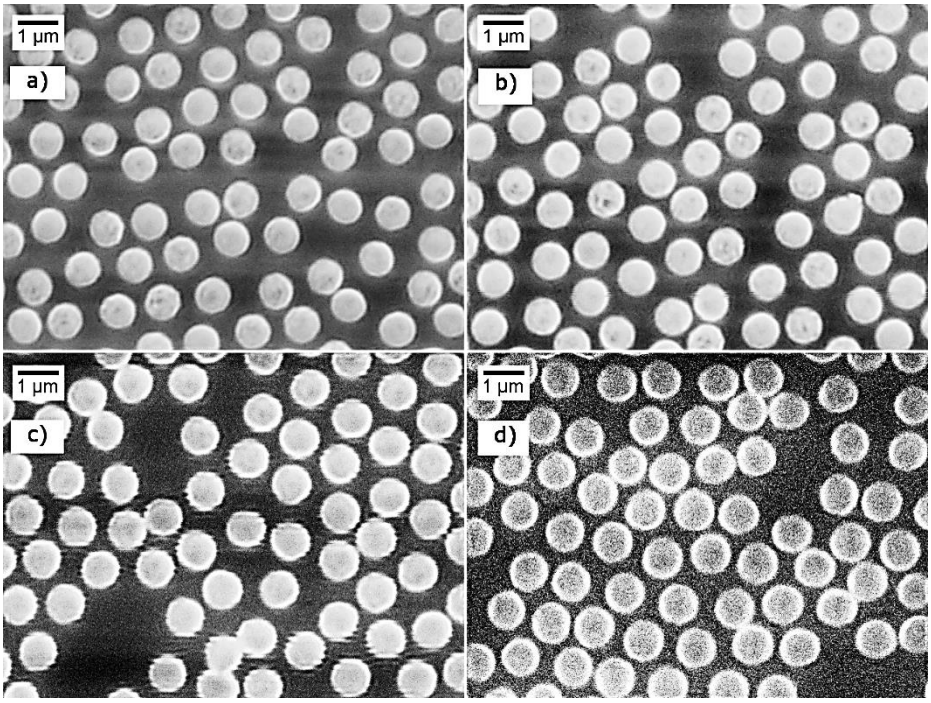

Figure 27 SEM images for the samples prepared with 120 s of etching time and varying etching pressures. a) 200 mTorr. b) 225 mTorr. c) 250 mTorr. d) 275 mTorr.

At this point, the quality of sphere deposition was not optimized and therefore a very poor deposition was conducted, which makes it harder to measure the actual spacing between spheres. To work around this problem the sphere diameter after the etching was measured instead of the spacing between the spheres.

Table 20: Average sphere diameter obtained for samples produced under 120 s of etching and varying etching pressures.

Sample (120 s etching)	*200 mTorr*	*225 mTorr*	*250 mTorr*	*275 mTorr*
Sphere diameter after etching (µm)	0,912	0,940	0,967	1,009

From these results and considering the original 1.3 μm diameter of the spheres we can conclude that even at 275 mTorr, 120 s is too much to produce a mesh with 100 nm linewidth. In future samples, the minimum pressure used was 250 mTorr.

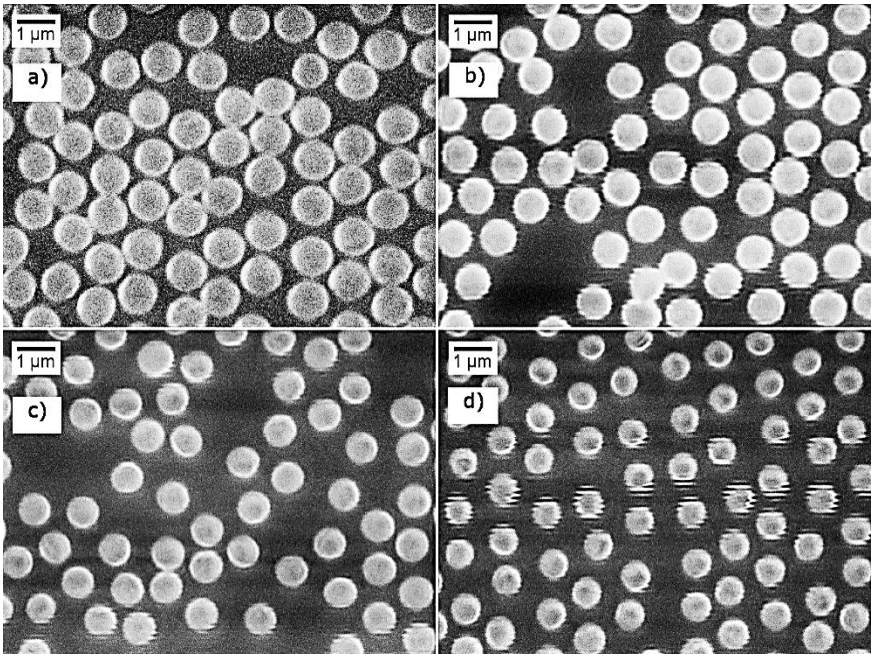

Figure 28 SEM images for the samples prepared with spheres with 1.3 μm spheres in an O_2 atmosphere of 250 mTorr and O_2 flow of 20 sccm, 90 W RIE power and varying etching times. a) 90 s. b) 120 s. c) 150 s. d) 180 s.

Table 21: Average sphere diameter obtained for samples produced under 250 mTorr etching pressure and varying etching times.

Sample (250 mTorr etching)	*90 s*	*120 s*	*150 s*	*180 s*
Sphere diameter after etching (μm)	1.104	0.967	0.874	0.799

After testing with 1.3 μm, one trial with 1.6 μm spheres was also conducted. For this trial we prepared 4 samples with fixed 120 s of etching time and varying etching pressures. One sample was not subjected to etching and the other three were subjected to 225, 250 and 275 mTorr etching pressures.

As can be seen by comparing the depositions in Figure 28 with the depositions in Figure 29, there is a clear difference in quality of sphere deposition between 1.3 μm and 1.6 μm spheres, even at early stages. Once again, the final sphere diameter was measured to reach the best conditions needed to obtain a mesh with 100 nm of width.

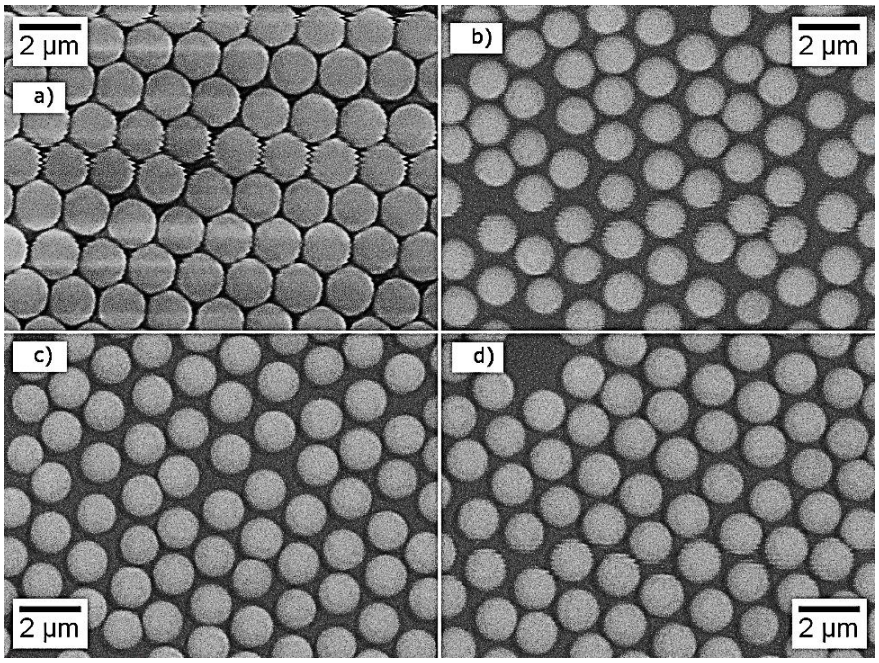

Figure 29 SEM images for the samples prepared with 1.6 µm spheres in an O_2 atmosphere of varying pressures, O_2 flow of 20 sccm, 90 W RIE power and 120 s of etching. a) No etching. b) 225 mTorr. c) 250 mTorr. d) 275 mTorr.

Table 22: Average sphere diameter obtained for samples produced under 120 s etching time and varying etching pressures.

Sample (120 s etching)	*Ref*	*225 mTorr*	*250 mTorr*	*275 mTorr*
Sphere diameter after etching (µm)	1.567	1.306	1.322	1.381

Again, the conditions used would produce a mesh with linewidth larger than 100 nm, so another batch of samples was produced with lower etching times. This time we fixed the pressure at 250 mTorr and used 4 different etching times, 30 s, 60 s, 90s and 120 s. This way the highest mesh width possible should be around 180 nm, as we saw in Table 22, allowing the production of a 100 nm conductive meshes.

Besides the deposition shown in Figure 30 d), good quality depositions were achieved. These images should allow us to extrapolate good etching conditions to obtain the intended mesh linewidth.

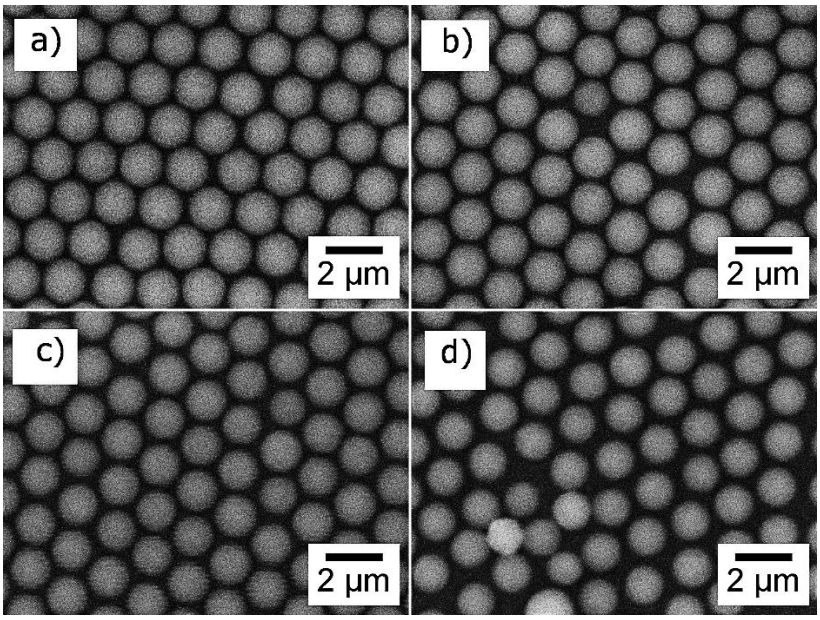

Figure 30 SEM images for the samples prepared with 1.6 µm spheres in an O_2 atmosphere of 250 mtorr, O_2 flow of 20 sccm, 90 W RIE power and varying etching times. a) 30 s. b) 60 s. c) 90 s. d) 120 s.

Table 23: Average sphere diameter obtained for samples produced under 250 mtorr etching pressure varying etching times.

Sample (120 s etching)	*30 s*	*60 s*	*90 s*	*120 s*
Sphere diameter after etching (µm)	1.555	1.479	1.451	1.401

Comparing the sphere diameter obtained for the sample with 120 s and 250 mTorr, we notice quite a difference from the previous value. This is due to both noise in the SEM image and poor resolution in the measurement of sphere diameter. Nonetheless, this should still give a decent approximation to the mesh linewidth. The sample with just 30 s should produce a mesh with 100 nm width, however, after depositing metal we checked the electrical properties and it was not conductive.

This test allowed us to establish a critical time necessary to produce conductive meshes, but in later tests we found that even 60 s can show some issues with electrical properties. Only 60 s of etching is not enough to allow many wires to be formed and great sheet resistance variation was seen in samples produced with this etching time. Therefore, at least 90 s etching is recommended.

B. Study of toluene bath for the removal of spheres

After the metal deposition, the spheres need to be removed to form the micromesh. This process is done through a toluene bath using ultrasounds. In this section we studied 4 different bath times to obtain the minimum time necessary to remove all spheres.

Figure 31 c) and Figure 31d) show no spheres, however, as was seen in previous SEM images in chapter IV, even with 15 min of toluene bath in ultra sounds some PS spheres are still present. Some

IPA testing was conducted showing comparable results to toluene. Samples can be subjected to longer ultra sound baths in IPA to try to remove all spheres.

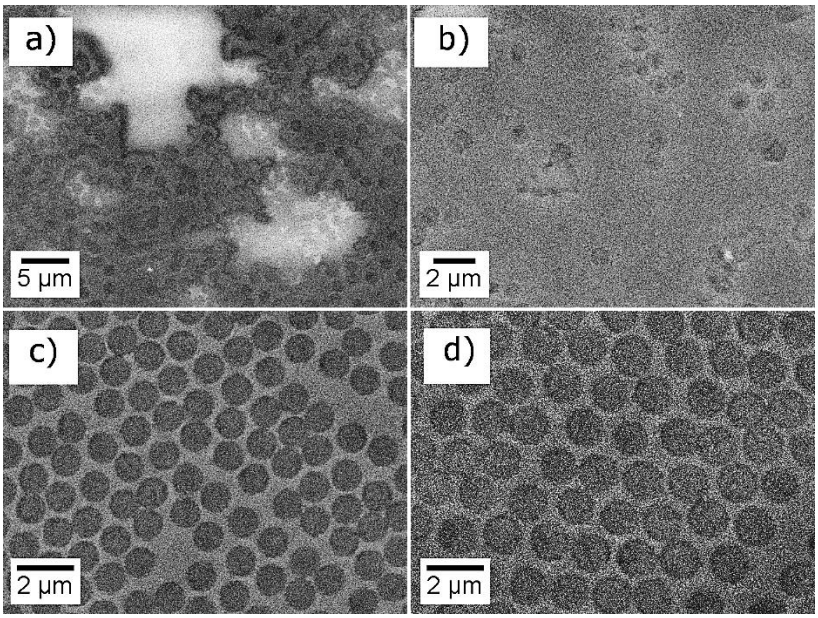

Figure 31 SEM images of samples after toluene bath. a) 1 min of toluene bath in ultra sounds. b) 3 min of toluene bath in ultra sounds. c) 5 min of toluene bath in ultra sounds. d) 15 min of toluene bath in ultra sounds.

C. Energy dispersive spectroscopy results

As stated in chapter 4.8, an EDS characterization of the samples was conducted. The SEM image showing the characterization sites and respective EDS graphs can be seen below (Figure 32 to Figure 34).

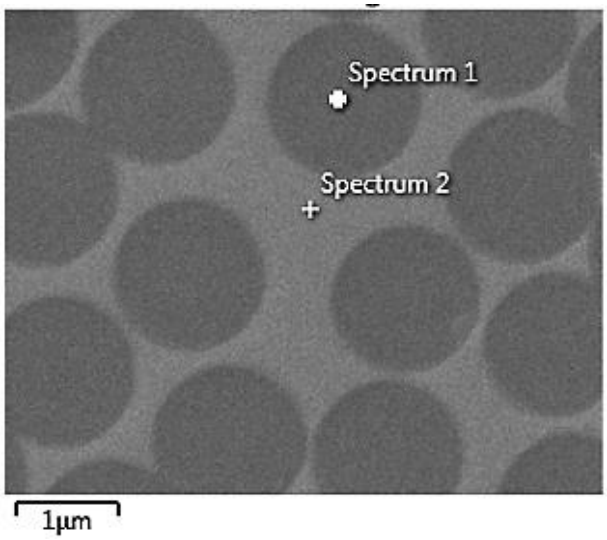

Figure 32: SEM image showing the sites where the EDS characterizations were conducted

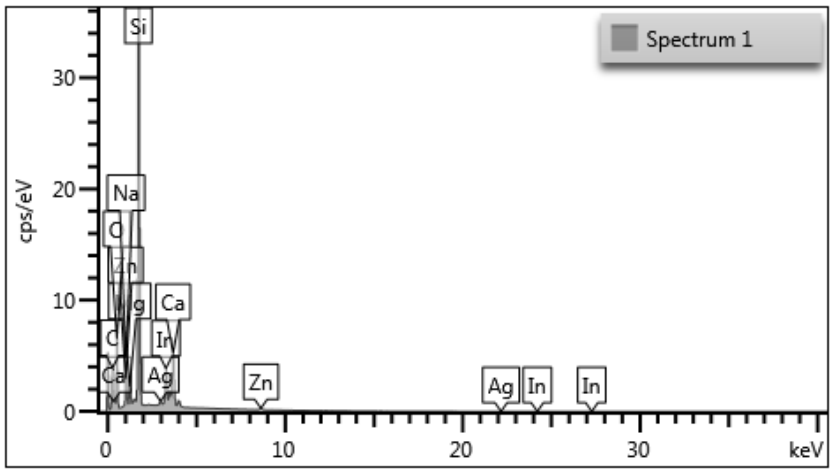

Figure 33: Plot of the EDS characterization conducted inside a hole (spectrum 1 shown on Figure 32)

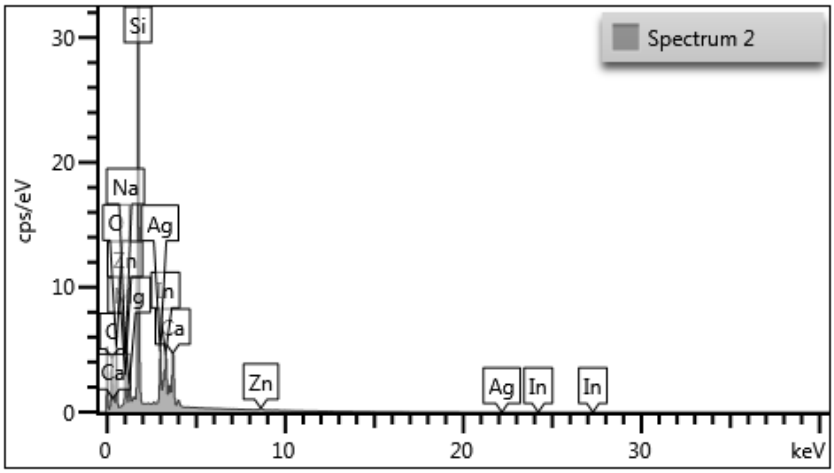

Figure 34: Plot of the EDS characterization conducted inside a hole (spectrum 2 shown on Figure 32)

D. Contact improvement study

Three samples were prepared, consisting of a sample with flat 15 nm film of silver in between two 30 nm thick IZO layers, one sample with structured silver in between two IZO layers and one where both the silver layer and the upper IZO layer were structured. The IZO was structured in the same way as the silver, meaning the second IZO deposition is conducted before the removal of the spheres. Both structured samples were fabricated using 1.6 µm spheres. The silver thickness was chosen to be 15 nm to avoid the formation of a film like the one in Figure 17.

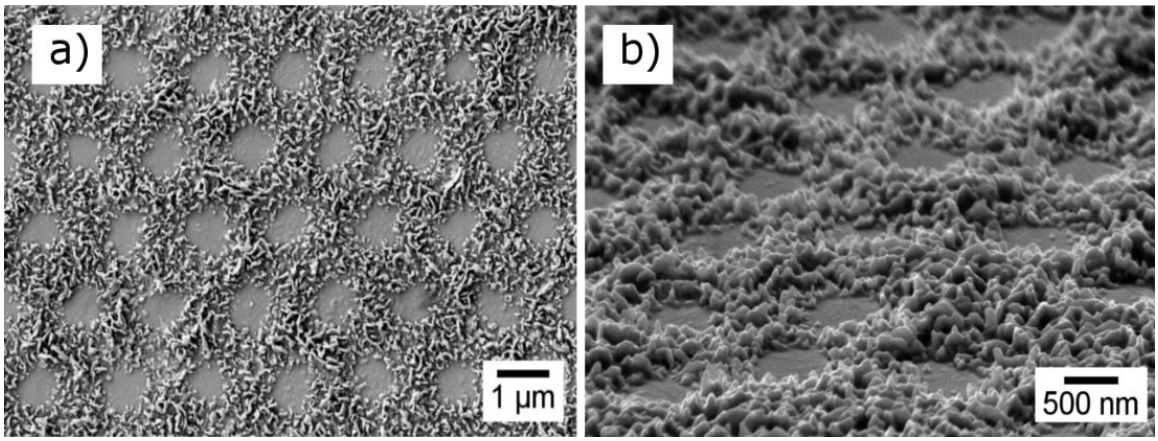

Figure 35 SEM image of the sample produced with 15nm of structured silver and 30 nm of structured IZO. a) Top view of the contact. b) Tilted view of the contact at an angle of 30 º.

This sample had good sphere deposition, however the silver deposition did not form a uniform mesh.

All samples and an extra sample with just 60 nm of IZO were characterized by spectrophotometer and hall-effect. However, due to the spectrophotometer used in previous characterizations being under repair, an older model had to be used. This equipment cannot measure the total transmittance for wavelengths higher than 800 nm.

The second dry etching was so destructive to the contact that even a sample with only IZO performed almost 13 times better. The sample with structured silver and IZO showed superior performance electrically and optically, despite the poor silver deposition. Future depositions as these ones should be conducted to obtain more accurate results.

From the spectrophotometer results seen in Figure 36 and Figure 37, we can see that the sample produced with structured silver and IZO has similar behavior to previous samples produced with 1.6 µm spheres. A noticeable difference in total transmittance and direct transmission can be seen for this sample in Figure 37 for wavelengths higher than 450 nm, which indicates that the sample has a much better behavior in the near infrared region than is shown.

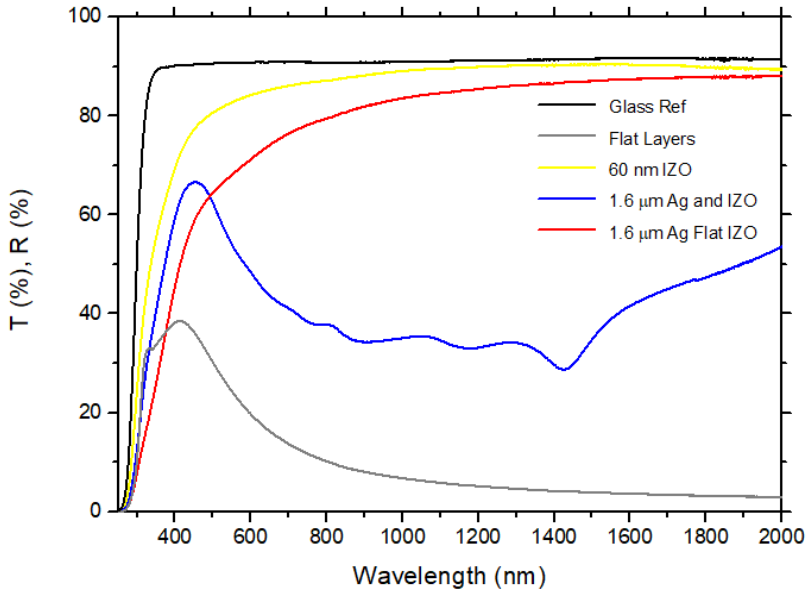

Figure 36 Spectrophotometer results for the direct transmittance of the different samples used.

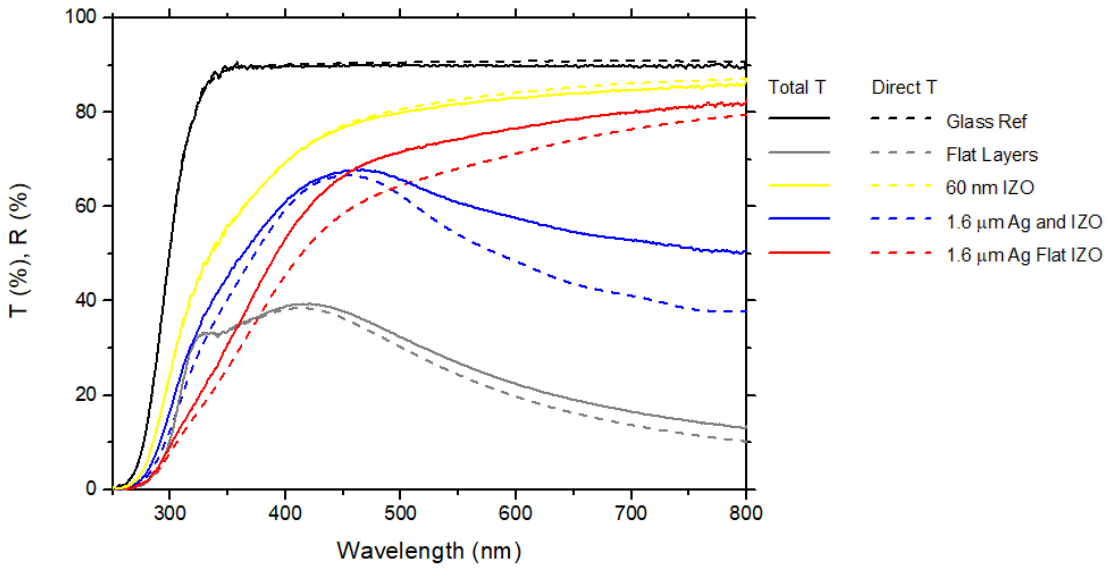

Figure 37 Spectrophotometer results comparing total transmittance and direct transmittance.

Lastly, some samples were prepared without any TCO layer. however, it was noticed that the sphere deposition was improved by a bottom TCO layer and a top TCO layer is necessary for encapsulation.